A hybrid VOF-IBM method for the simulation of freezing liquid films and freezing drops

Sijia Lyu, Ke Wang, Zhentong Zhang, Annaïg Pedrono, Chao Sun, Dominique Legendre

Contents lists available at ScienceDirect

Journal of Computational Physics

journal homepage: www.elsevier.com/locate/jcp

A hybrid VoF-IBM method for the simulation of freezing liquid films and freezing drops

Sijia Lyu[a,b], Ke Wang[b], Zhentong Zhang[b], Annaïg Pedrono[b], Chao Sun[a], Dominique Legendre[b,*]

[a] *Center for Combustion Energy, Key Laboratory for Thermal Science and Power Engineering of Ministry of Education, Department of Energy and Power Engineering, Tsinghua University, 100084 Beijing, China*
[b] *Institut de Mécanique des Fluides de Toulouse (IMFT), Université de Toulouse, CNRS - Toulouse, FRANCE*

ARTICLE INFO

Article history:

Icing, Liquid film, Drop, VoF-IBM

ABSTRACT

This work is devoted to the development of a new hybrid VoF-IBM method for the simulation of freezing liquid films and freezing drops. The VoF and IBM methods are coupled with the temperature equation to be able to solve the icing front, the dilatation induced by the density difference between the liquid and the ice as well as the drop deformation induced by the balance of the surface tension and gravity. The numerical simulations are validated by a comparison between the theoretical solutions and experimental observations. We investigate the effect of the Stefan number and the ratio of solid density to liquid density on the height evolution of the icing front for both liquid films and drops. We also study the whole freezing processes of drops with different contact angles. Furthermore, the effect of gravity and the surface tension on freezing processes of drops are investigated. The temperature distribution, solidification shape, and evolution within the drop are systematically analyzed and the CSF-VoF spurious currents are shown to induce no effect on the icing process due to the small value of both the corresponding Weber and Capillary numbers. We find that the final drop shape is in very good agreement with experiments, and in particular the value of the tip angle of the iced drop and the front-to-interface angle are very well reproduced.

1. Introduction

Supercooled water cloud, freezing frog and freezing rain interaction with cold surfaces can cause severe hazards for the daily life and many industrial processes, for example attaching and destructing the power

*Corresponding author, Email address: dominique.legendre@imft.fr

cables, increasing the weight and changing the streamlines of the aircrafts, ships and the wind turbines, reducing the friction of cars on roads, and even resulting in severe disasters. Therefore, many efforts have been devoted to understand the nucleation of icing and to develop de-icing techniques.

Icing of a single drop is a fundamental problem. However, even for this basic problem, there are still some challenges for both experimental and numerical investigations. A large amount of experimental works have been tried to provide a complete description of the icing of a drop [1, 2, 3, 4, 5]. However, experimental approaches have to face to some issues. Chaudhary *et al.* [6] used an IR camera and three thermocouples to measure the topmost temperature on the substrate and the temperature evolution of three different points inside the drop. The authors were able to identify four steps involved during the process: liquid cooling, recalescence, freezing and solid cooling, but the presence of the thermocouples probes are responsible of local nucleation resulting of different sources of recalescence. Nauenberg [7] has outlined the importance of the substrate temperature control for the icing process. In addition, frost crystals can grow on the droplet surface and the cold substrate and can complexify the measurments [8]. People can get outside information and part of the local inner information of freezing drops by experimental methods. However, it is challenging to obtain the detailed information of the inner icing front, the temperature field and induced heat fluxes, velocity and pressure distributions inside the drop and ice. In addition, the intrusive measurements may cause some additional nucleation sites and consequently influence the icing process, and the non-intrusive methods are difficult to access the detailed dynamics inside the drop. Furthermore, the frost crystals caused by the vapor in the surroundings are hard to completely avoid, posing additional challenges for optical measurements.

Thus, it's very relevent to develop accurate numerical methods to obtain comprehensive inner information of freezing water drops. Some studies on the solidification of alloy have focused on the dendritic growth [9]. For the solidification of standard liquids such as water, much numerical research mainly consider the heat conductivity problems with possible non-linear physical properties to analyze the solidification process [10, 11, 12, 13, 14]. However, the simplifications in these numerical methods and models could cause differences between the experimental and numerical results. Chaudhary *et al.* [6] numerically solved the enthalpy-based heat conductivity equation to provide insight into the heat transfer during the cooling and freezing process, but they don't consider the density difference between water and ice. Vu *et al.* [15] propose a front-tracking method that includes the volume expansion for the simulation of liquid drop on a cold surface for a fixed contact angle of 90^o. In Zhang *et al.* [16], the VoF multiphase model is coupled with the solidification model in Fluent 14.0 to simulate the freezing of water droplets. However, the deformation of the liquid is ignored. Recently, Tembely *et al* [17] enable to model a more realistic frozen droplet shape, but their model is mainly valid for hydrophilic drops. Some numerical approach have recently coupled IBM and sharp interface methods for the simulation of drop standing on solid surface [18, 19]. These motivate us to propose an efficient and wide applicable numerical method to perform accurate simulations of freezing films and drops with varying wetability conditions.

In this way, we develop a new fully direct numerical approach based on a hybrid VoF-IBM method, which considers the coupling between the heat transfer and phase change, the volume expansion due the density difference between the ice and the liquid, and surface tension effects at the gas-liquid interface. Some simple and practical cases, such as liquid films and drops, are used to show the applicable range of the numerical method. We validate the numerical simulations with the comparison to theoretical solutions and experimental observations. The temperature, velocity and pressure distributions inside the drop are also displayed, which can be used for further benchmarking for code comparison and validation.

The paper is organized as follows. The numerical method is described in section 2. The verification and validation of the method by the liquid film model are presented in section 3. Several parameters that affect the freezing rate are investigated, such as the Stefan number, the ratio of solid density to liquid density. Section 4 reports the solidification of a liquid film in a 2D container. The freezing drop without surface tension and gravity is presented in section 5. The hydrophilic and hydrophobic freezing drops illustrate the wide applied range of this method. In section 6, the gravity and the surface tension are supplied to the freezing drop. These numerical results are consistent with experiments, which means that the surface tension is a key factors for the freezing of a drop. The conclusion is reported in section 6.

2. Equations and Numerical method

The objective of the numerical method is to be able to simulate the propagation of a freezing front in a liquid in contact with a cold wall. In the following T_m will be the melting temperature and the solidification front will match the isotherme $T = T_m$. Once iced the solid velocity $\mathbf{U}_s$ will be imposed equal to the wall velocity.

The proposed numerical method developed in the JADIM code consists in coupling a Volume of Fluid (VoF) solver [20, 21, 22] used to tack the liquid/gas interface with an IBM approach [23] for the simulation of the solid phase. In the following the subscript l, g and s will be used to denote the liquid, gas and solid phases, respectively.

2.1. The VoF function and ice fraction

The VoF function C is used to localize the liquid-gas interface. $C = 1$ in the liquid phase and $C = 0$ in the surrounding gas. The position of the liquid-gas interface is then given by the transport equation:

$$\frac{\partial C}{\partial t} + U \cdot \nabla C = 0. \tag{1}$$

The solid phase is described using the ice fraction g such that $g = 1$ in the solid, and $g = 0$ in the fluids for both liquid and gas. The evolution of g is governed by the equation

$$\frac{\partial g}{\partial t} + \mathbf{V}_s \cdot \nabla g = 0, \tag{2}$$

where $\mathbf{V}_s$ is the velocity of the solidification front between the solid and the liquid. In the following, the normal of the solidification front (from the ice to the liquid) is noted $n_s = -\nabla g/|\nabla g|$. The value of C remains $C = 1$ once the liquid has been changed into ice and the reason will be cleared later.

From the VoF function C and the ice fraction g, we introduce the 1-phase quantities that will be considered in the numerical resolution. The physical properties such as density, viscosity, thermal conductivity and heat capacity will be defined by $\rho = (1-C)(1-g)\rho_g + C(1-g)\rho_l + Cg\rho_s$, $\mu = (1-C)(1-g)\mu_g + C(1-g)\mu_l$, $\lambda = (1-C)(1-g)\lambda_g + C(1-g)\lambda_l + Cg\lambda_s$ and $C_p = (1-C)(1-g)C_{pg} + C(1-g)C_{pl} + CgC_{ps}$ and the variables velocity, pressure and temperature will be defined by $\mathbf{U} = (1-C)(1-g)\mathbf{U}_g + C(1-g)\mathbf{U}_l + Cg\mathbf{U}_s$, $P = (1-C)(1-g)P_g + C(1-g)P_l$ and $T = (1-C)(1-g)T_g + C(1-g)T_l + CgT_s$.

The hybrid VoF-IBM method presented below consists in solving the system of equations satisfied by these 1-phase quantities.

2.2. The Temperature equation

The temperature equation used to follow the solidification front is derived from the enthalpy conservation. The objective is to solve an equation for the 1-phase temperature defined with the VoF and ice functions. The enthalpy in the three phases, gas, liquid and solid (ice) phases are respectively given by $H_g = C_{pg}(T_g - T_m)$, $H_l = C_{pl}(T_l - T_m) + L$ and $H_s = C_{ps}(T_s - T_m)$, here L is the latent heat and T_m is taken as the temperature of reference. In the following the conductivities, latent heat, heat capacities for the gas, liquid and solid phases will be considered to be constant.

Based on these expressions the 1-phase enthalpy $H = (1-g)(1-C)H_g + (1-g)CH_l + gCH_s$ satisfies the conservation equation

$$\frac{\partial \rho H}{\partial t} + \nabla \cdot (\rho H \mathbf{U}) = \nabla \cdot (\lambda \nabla T)\,. \tag{3}$$

From Eq. 3, it follows the equation satisfied by the 1-phase temperature T:

$$\rho C_{p,\,app}\frac{\partial T}{\partial t} + \nabla \cdot (\rho C_p T \mathbf{U}) = \nabla \cdot (\lambda \nabla T)\,, \tag{4}$$

where an equivalent heat capacity $C_{p,\,app}$ has been formed [11, 24]:

$$\rho C_{p,\,app} = \rho C_p + (\rho_s C_{ps} - \rho_l C_{pl})(T - T_m)\frac{dg}{dT} - \rho_s L \frac{dg}{dT}. \tag{5}$$

The great interest of this formulation is to make implicit the calculation of the source term at the ice front coming from the latent heat considering

$$\frac{\partial g}{\partial t} = \frac{dg}{dT}\frac{\partial T}{\partial t}$$

A smooth transition between ice and liquid needs to be introduced for the stabilization of the numerical resolution of the temperature equation [11, 24]. Such approach introduces an equivalent melting region and the solidification front diffusion during the solidification is controlled by the g function. We introduce $T_{min} < T_m$ and $T_{max} > T_m$ the range of temperature where solidification occurs. Instead of solving Eq. 2 for g, g is defined as a function of the temperature T to make possible the regularization of the transition

from the ice ($g = 1$ for $T \leq T_{min}$) to the fluid ($g = 0$ for $T \geq T_{max}$). The following functions g_i shown in Fig. 1 will be considered and compared in this study:

$$g_1(T) = \frac{T_{max} - T}{T_{max} - T_{min}} \quad \text{if} \quad T_{min} < T < T_{max}, \tag{6}$$

$$g_2(T) = \left(\frac{T_{max} - T}{T_{max} - T_{min}}\right)^5 \quad \text{if} \quad T_{min} < T < T_{max}, \tag{7}$$

$$g_3(T) = \frac{1}{2}\left(1 + \tanh\frac{p(T - T_m)}{T_{max} - T_{min}}\right), \tag{8}$$

where p is used to define the size of the melting region. The interest of these relations is to give an exact expression for dg/dT to consider in Eq. 5. These functions g_i will be tested and compared in section 3.3 and the effect of $\Delta T = T_{max} - T_m = T_m - T_{min}$ will be discussed.

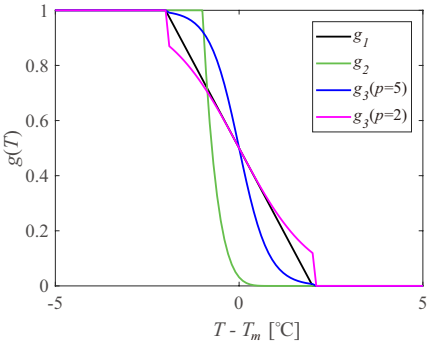

Fig. 1. Different g functions versus temperature difference $T - T_m$.

2.3. The coupled VoF and IBM system of equation

The hybrid VoF-IBM system of equation is considered for two Newtonian and incompressible fluids and a solid phase (the ice) with constant physical properties (viscosity, density, surface tension) and no phase change at the liquid-gas interface.

2.3.1. Mass conservation

Resulting from the change of density from liquid to solid (here $\rho_s < \rho_l$), the ice displaces the liquid at the solidification front. The corresponding velocity for the liquid resulting from the mass conservation at the icing front is then

$$\mathbf{U}_l \cdot \mathbf{n}_s = \mathbf{V}_s \cdot \mathbf{n}_s \left(1 - \frac{\rho_s}{\rho_l}\right). \tag{9}$$

The mass conservation expressed using the 1-phase velocity $\mathbf{U}$ is

$$\nabla \cdot \mathbf{U} = -C\, \mathbf{U}_l \cdot \nabla g. \tag{10}$$

Considering relations 2 and 9, the mass conservation is then

$$\nabla \cdot \mathbf{U} = C\left(1 - \frac{\rho_s}{\rho_l}\right)\frac{\partial g}{\partial t}. \tag{11}$$

2.3.2. Momentum conservation

The momentum conservation is derived to integrate both the VoF formulation for the capillary contribution and an IBM penalization inside the solid. The resulting momentum equation is

$$\rho\left(\frac{\partial \mathbf{U}}{\partial t}+\mathbf{U}\cdot\nabla\mathbf{U}\right)=-\nabla P+\nabla\cdot\Sigma+\rho\mathbf{G}+\mathbf{F}_{\sigma}+\mathbf{F}_{IBM}, \tag{12}$$

with Σ is the viscous stress tensor and G is the gravity.

$\mathbf{F}_{\sigma}$ is the capillary contribution at the liquid gas interface calculated using the Continuum Surface Force method previously described in [25, 20, 26]:

$$\mathbf{F}_{\sigma}=\sigma\nabla\cdot\left(\frac{\nabla C}{||\nabla C||}\right)\nabla C, \tag{13}$$

where σ is the surface tension. The method used to consider static and moving contact line is described in [20, 22, 27]. In the situation of icing, Vahab *et al.* [28] impose an angle between the three phases by considering the three surface energies. The resulting simulations of freezing droplets clearly show a change of the drop shape at the freezing triple point. In our approach, the angle between the liquid-ice-air on the freezing front is not imposed but results from the local solidification isotherm $T=T_m$ so that it is controlled by the balance of the heat fluxes from the three phases. As observed in the reported simulation of freezing drops, this induces no shape variation (i.e. the curvature and the normal are not changed) when the liquid is transformed into ice. Such condition is supported by experiments where no noticeable change of the drop shape curvature is observed at the ice front location [1, 3]. For that purpose the value of the VoF function C is kept equal to $C=1$ when the liquid is transformed into ice.

$\mathbf{F}_{IBM}$ is the IBM forcing term given by

$$\mathbf{F}_{IBM}=\chi\frac{\mathbf{U}_s-\mathbf{U}}{\Delta t}, \tag{14}$$

where $\mathbf{U}_s$ is the local velocity imposed for the solid phase and χ is called solid volume fraction or IBM function, which equals one in cells filled with the solid phase, zero in cells filled with the fluid phase, and $0<\chi<1$ in the region of the boundary. In practice, the transition region is imposed to be of one-to-three grid cells [23, 29]. This approach has been selected compared to methods using a regularizing function in conjunction with a Lagrangian marking of the boundary [30, 31] because it is simple to implement and to couple with the regularization of the temperature equation, and it has been shown to be in good agreement with respect to other available higher-order immersed-boundary or boundary fitted approaches [23].

2.3.3. Coupling between the methods

As indicated above, the solidification front corresponds to the isotherm $T=T_m$ so that the IBM function χ is directly related to the ice fraction g. Both the resolution of the temperature equation and the IBM forcing require a regularization for the transition from the solid where $\chi=g=1$ to the liquid where $\chi=g=0$. In our approach we simply couple these functions as

$$\chi=g(T)\,C, \tag{15}$$

so that the same regularization is used for the two resolutions.

2.4. Discretization and overall algorithm

The system of equations presented above is discretized on a staggered grid using a finite volume method, all spatial derivatives being approximated using second-order centered schemes. The VoF function C, the ice fraction g, the IBM function χ and the pressure P are volume-centered while the velocity components are face-centered. Time advancement for both the momentum and temperature equations is achieved through a third-order Runge-Kutta (RK3) method for advective and source terms and a Crank-Nicolson method for the diffusive terms. Incompressibility is satisfied at the end of each time step though a projection method. The overall algorithm was developed to be second-order accurate in both time and space. The accuracy of the hybrid VoF-IBM method developed here for icing problems will be discussed in the next section.

The calculation is initialized with the initial gas-liquid interface and no solidification front is present. The frozen process is generated by the temperature diffusion from a cold wall with an imposed temperature less than T_m. Basically each time step is composed of four steps. Hence starting with $\mathbf{U}^n$, $P^{n-1/2}$, C^n and g^n they are:

Step 1. Update value for C^{n+1}

The advection equation (1) for the VoF function is solved by using the FCT transport scheme described in detail in [25].

Step 2 Update value for T^{n+1} and $\mathbf{U}^*$

In this RK3 time-stepping procedure, an intermediate velocity field $\mathbf{U}^*$ and the final temperature field T^{n+1} are computed from changes to the known field $\mathbf{U}^n$ and T^n, respectively. The advective terms A and A_T are computed explicitly while the diffusive terms L and L_T are treated using the semi-implicit Crank-Nicolson algorithm [32, 33]. Within each of the three intermediate steps ($k = 1, 2, 3$) of the time step $[n\Delta t, (n+1)\Delta t]$ the solution is advanced as follows where $T^{k=0} = T^n$, $T^{n+1} = T^{k=3}$, $\mathbf{U}^{k=0} = \mathbf{U}^n$ and $\mathbf{U}^* = \mathbf{U}^{k=3}$. We note $g^k = g(T^k)$ the value of the ice fraction. The Runge-Kutta coefficients ξ_k, β_k, γ_k and ζ_k are those used in the RK3/CN algorithm detailed in [32].

Step 2a. Update value for the physical properties

The intermediate value $C^{n+1/2}$ of the volume fraction is used with the ice fraction g^{k-1} to obtain the physical properties ρ^k, μ^k, $C^k_{p,app}$ and λ^k used in each RK3 step.

Step 2b. Update value for T^k

The equation for the temperature is solved with

$$\rho^k C^k_{p,\,app}\frac{T^k - T^{k-1}}{\Delta t} = \gamma_k A_T(T^{k-1}) + \zeta_k A_T(T^{k-2}) + (\xi_k + \beta_k)L_T(T^{k-1}) + \beta_k L_T(T^k - T^{k-1}) \qquad (16)$$

This equation being discretized using the finite volume method, the term $\rho^k C^k_{p,\,app}$ is calculated at the cell center while $\rho^k C^k_p$ involved in the advective terms A_T and λ^k involved in the diffusive terms L_T are calculated at the cell face's center with the value of g^{k-1} calculated using the temperature T^{k-1} interpolated at the cell faces' center.

Step 2c. Intermediate value $\tilde{\mathbf{U}}^k$

Calculation of an intermediate velocity field $\tilde{\mathbf{U}}^k$ from the discretization of the momentum equation 12 without considering the IBM and capillary terms:

$$\frac{\tilde{\mathbf{U}}^k - \mathbf{U}^{k-1}}{\Delta t} = SM^{k-1}, \tag{17}$$

with

$$SM^{k-1} = \gamma_k A(\mathbf{U}^{k-1}) + \zeta_k A(\mathbf{U}^{k-2}) + (\xi_k + \beta_k)\left[\mathbf{G} - \frac{1}{\rho^{n+1/2}}\nabla P^{n-1/2}\right] + (\xi_k + \beta_k)L(\mathbf{U}^{k-1}). \tag{18}$$

Step 2d. Update value for the velocity field $\mathbf{U}^k$

Modification of the velocity field to include the coupling between the solid and the fluids. The IBM interaction is computed using the update IBM function $\chi^k = g^k C^{n+1}$ in order to obtain the IBM forcing term

$$\mathbf{F}^k_{IBM} = \chi^k \frac{\mathbf{U}_s - \tilde{\mathbf{U}}^k}{\Delta t}, \tag{19}$$

used to calculate the update value $\mathbf{U}^k$ as

$$\frac{\mathbf{U}^k - \mathbf{U}^{k-1}}{\Delta t} = SM^{k-1} + \beta_k L(\mathbf{U}^k - \mathbf{U}^{k-1}) + \mathbf{F}^k_{IBM}. \tag{20}$$

Note that no internal loop is used here following Bigot et al. [23].

Step 3. Capillary contribution for $\mathbf{U}^{**}$

A second intermediate velocity field $\mathbf{U}^{**}$ is introduced to correct $\mathbf{U}^*$ in order to include the capillary contribution given by (13)

$$\frac{\mathbf{U}^{**} - \mathbf{U}^*}{\Delta t} = \frac{1}{\rho^{n+1/2}}\mathbf{F}^{n+1/2}_\sigma. \tag{21}$$

The discretization of $\mathbf{F}^{n+1/2}_\sigma$ using the finite volume method is described in detail in [27].

Step 4. Projection step for $\mathbf{U}^{n+1}$

The final velocity field $\mathbf{U}^{n+1}$ is finally computed to satisfy equation (11) by solving

$$\frac{\mathbf{U}^{n+1} - \mathbf{U}^{**}}{\Delta t} = -\frac{1}{\rho^{n+1/2}}\nabla\Phi^{n+1/2}, \tag{22}$$

where the pressure correction $\Phi^{n+1/2}$ is the solution of the pseudo-Poisson equation with the phase change contribution at the ice front

$$\nabla\cdot\left(\frac{1}{\rho^{n+1/2}}\nabla\Phi^{n+1/2}\right) = \frac{\nabla\cdot\mathbf{U}^{**}}{\Delta t} - \frac{1}{\Delta t}C^{n+1}\left(1 - \frac{\rho_s}{\rho_L}\right)\frac{g^{n+1} - g^n}{\Delta t}. \tag{23}$$

The final pressure is deduced from the auxiliary potential $\Phi^{n+1/2}$ through the relation

$$P^{n+1/2} = P^{n-1/2} + \Phi^{n+1/2}. \tag{24}$$

Step 5. return to Step 1.

3. Verification and Validation

JADIM code has been extensively used and validated for numerical studies of bubbles, drops and particles dynamics [34, 33, 35, 36, 37, 38, 39]. In particular the VoF method has been used for the simulation of sessile drop [20, 40, 22] and the IBM method for solid particle motion [23]. Here, we couple the VoF and IBM methods for the simulation of the icing of static liquid films and drops. The validation presented here considers the 1D Stefan problem and mainly focuses on the coupling of the heat transfer, the phase change, the solidification front motion and the motion of the liquid pushed by the solidification front resulting from density change.

3.1. Statement of the theoretical 1D Stefan problem

The term "Stefan problem" is generally used for heat transfer problems with phase-changes such as from liquid to solid [41, 42, 43, 44]. In the hyperbolic Stefan problems, the characteristic features of Stefan problems are present but unlike the classical ones, and discontinuous solutions are allowed because of the hyperbolic nature of the heat equation. The problem is the boundary value of a partial differential equation (PDE), characterized by two regions, one for each of the two phases, in which the solutions of the underlying PDE are continuous and differentiable. But there is also an interface region, characterized by a discontinuity, where another condition (Stefan's condition) is applied in order to obtain closure. Peculiarity of the problem is the fact that the position of the interface evolving in time is a variable itself, so the boundary conditions are applied with respect to a time dependent position, unknown a priori.

In order to obtain a theoretical solution, some simplifications need to be made, which are reasonable for pure materials in case of moderate thermal gradients and temperatures: (i) The heat transfer is driven by the conduction and convection, assuming negligible radiative transfer; (ii) Sharp and local plane interface; (iii) Thermophysical properties are constants with temperature in each phase, while they are different between two phases; (iv) Phase change temperature is fixed and known.

Considering a mono-dimensional and semi-infinite domain filled with phase-change material in the positive y-axis direction, at an initial temperature T_{li} greater than the melting one T_m, ($T_{li} > T_m$), which means there is no solidification in the beginning $t = 0$ s. The material is cooled by the wall at the position $y = 0$ and at a constant temperature T_w which is lower than T_m. When the temperature of the material decreases to the melting temperature, it freezes and releases the latent heat. Calling $h_s(t)$ the height of the interface between the liquid and the solid, and solving the system of equations for the temperature in this problem coupled with the solid dilatation due to the phase change, the velocity of the liquid v_l is resulting from Eq. (9) is

$$v_l = \frac{dh_s}{dt}\left(1 - \frac{\rho_s}{\rho_l}\right), \tag{25}$$

where t is the time, ρ_s and ρ_l are the density of the solid and that of the liquid. The temperature equations

of the solid phase $T_s(t,y)$ and the liquid phase $T_l(t,y)$ are as follows,

$$\frac{\partial T_s}{\partial t} = \alpha_s \frac{\partial^2 T_s}{\partial y^2} \quad 0 < y < h_s(t), \tag{26}$$

$$\frac{\partial T_l}{\partial t} + v_l \frac{\partial T_l}{\partial y} = \alpha_l \frac{\partial^2 T_l}{\partial y^2} \quad y > h_s(t), \tag{27}$$

where α_s and α_l are the thermal diffusivity of the solid and that of the liquid, and $\alpha = \lambda/(\rho C_p)$, λ is the conductivity and C_p is the specific heat capacity. The boundary conditions, initial conditions and the conditions of continuity are

$$\begin{cases} T_s(y=0,t) = T_w \\ T_l(y\to\infty,t) = T_{li} \\ T_s(y>0,t=0) = T_l(y>0,t=0) = T_{li} \\ T_s(y=h_s(t),t) = T_l(y=h_s(t),t) = T_m \\ \lambda_s \frac{\partial T_s}{\partial y} - \lambda_l \frac{\partial T_l}{\partial y} = \rho_s L \frac{dh_s}{dt} \\ h_s(t=0) = 0, \end{cases} \tag{28}$$

giving the evolution of the front position as

$$h_s(t) = 2\delta(\alpha_s t)^{1/2}, \tag{29}$$

where δ is a constant depending on the initial conditions. From the above equations, we can obtain the value of δ from

$$\frac{e^{-\delta^2}}{erf(\delta)} - \phi\alpha^{1/2} \frac{e^{-[\alpha^{1/2}\delta(1-r)]^2}}{erfc[\alpha^{1/2}\delta(1-r)]} = \frac{\delta\pi^{1/2}}{Ste}, \tag{30}$$

with $\alpha = \alpha_s/\alpha_l$, $\phi = [\lambda_l(T_i - T_m)]/[\lambda_s(T_m - T_w)]$, $r = 1 - \rho_s/\rho_l$ and the Stefan number $Ste = Cp_s(T_m - T_w)/L$. The temperature of solid and liquid phases are:

$$T_s(y,t) = T_w + (T_m - T_w)\frac{erf[\frac{y}{2(\alpha_s t)^{1/2}}]}{erf(\delta)} \quad 0 < y < h_s(t), \tag{31}$$

$$T_l(y,t) = T_i + (T_m - T_i)\frac{erfc[\alpha^{1/2}\delta(\frac{y}{2\delta(\alpha_s t)^{1/2}} - r)]}{erfc[\alpha^{1/2}\delta(1-r)]} \quad y > h_s(t). \tag{32}$$

The theoretical solution of this problem given by Eq. (29-32) will be called "theory" in the following when used for comparison with simulations.

3.2. Configuration of the freezing liquid film

We design a 1D numerical simulation shown in the Fig. 2(a-c) to study the solidification of the liquid film. We compare the numerical results with the theoretical solution to validate the accuracy of the hybrid method. In the simulation, the initial temperature of the liquid is also larger than the melting point. The liquid is also cooled by the bottom wall which is at a constant temperature. The difference between the theoretical problem and real numerical problem is that the volume of the liquid of the theoretical problem is infinite, but that of the simulation is limited. However, when the height of the solid is much smaller than

that of the liquid, the liquid can be approximately to be infinite. At this time scale, we can compare the result of the simulation with the theory. The settings of four walls in the 1D simulation are as follows, (a) for the north wall, it is the outlet and adiabatic; (b) for the west and east walls, they are under symmetry condition and adiabatic; (c) for the south wall, it is at the wall condition with the constant temperature. The parameters shown in the Fig. 2(a-c) have the following meanings, h_{li} is the the initial height of the liquid, $h_l(t)$ is the height of the liquid front as a function of the time, $h_s(t)$ is the height of the solid front as a function of the time, h_{se} is the final height of the solid front when all of the liquid freeze to the solid, $v_s = \mathrm{d}h_s(t)/\mathrm{d}t$ is the velocity of the solidification front, $v_l = \mathrm{d}h_l(t)/\mathrm{d}t$ is the velocity of the liquid front, T_w is the constant temperature of the south wall, T_{gi} is the initial temperature of the gas, T_{li} is the initial temperature of the liquid, $T_{gi} = T_{li}$, $T_s(y)$ is the temperature of the solid as a function of position, and the temperature of the solid $T_l(y)$ is a function of position.

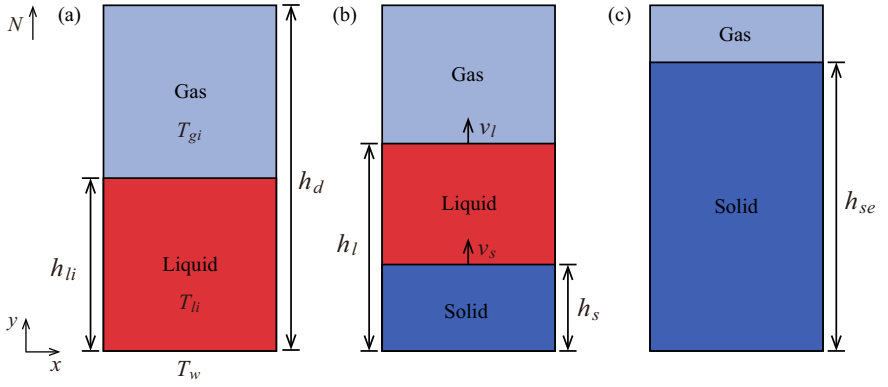

Fig. 2. Configuration of the freezing liquid film. (a) The initial phase before freeze, (b) the intermediate stage when part of the liquid freezes to the solid, (c) the final moment when all of the liquid freezes to the solid.

The initial height of the liquid $h_{li} = 10^{-3}$m; the temperature of the wall is $T_w = -20°$C; the initial temperatures of the liquid and that of the gas are $T_{li} = T_{gi} = 20°$C. In this paper, without a special explanation, the liquid, solid and gas represent water, ice and air, respectively. The physical properties are assumed to be constant without the temperature dependence shown in Table. 1. The solidification latent heat of water is 334 kJ/kg. The dimensionless grid spacing is the ratio between the grid spacing Δ to the initial height of the liquid h_{li}. The dimensionless time step is the ratio between the time step Δt to the heat diffusion time in the liquid $t_{diff} = h_{li}^2/\alpha_l = 7.58$ s.

Table 1. Physical properties of air, water and ice in our simulations

	ρ [kg/m^3]	μ [Pa·s]	α [m^2/s]	C_p [J/(kg°C)]
Air	1.29	1.70×10^{-5}	2.00×10^{-5}	1.00×10^{3}
Water	1.00×10^{3}	1.70×10^{-3}	1.32×10^{-7}	4.21×10^{3}
Ice	9.17×10^{2}	1.70×10^{-3}	1.18×10^{-6}	2.03×10^{3}

3.3. Different temperature transition functions $g(T)$

Four different g functions used to smooth the temperature transition from the solid to the liquid (see Fig. 1) are now tested and compared. The grid size and the time step are fixed to $\Delta/h_{li} = 1.25 \times 10^{-2}$ and $\Delta t/t_{diff} = 1.65 \times 10^{-5}$, respectively.

We use points at regular interval time to measure the errors between the numerical height h_k^{Δ} and the exact height h_k^{TH}. The normalized mean differences E_{ave}^{Δ} defined as

$$E_{ave}^{\Delta} = \frac{1}{k}\sum_{k}\left(\left|h_k^{\Delta} - h_k^{TH}\right|/h_k^{TH}\right), \tag{33}$$

are compared in the Table. 2 for the range $h_s < 0.1h_{li}$. The error is also reported for different values of $\Delta T = T_{max} - T_m = T_m - T_{min}$.

Table 2. The normalized mean differences E_{ave}^{Δ} for different g functions

ΔT [°C]	g_1	g_2	$g_3(p{=}5)$	$g_3(p{=}2)$
0.5	6.03×10^{-3}	5.06×10^{-2}	1.31×10^{-2}	2.97×10^{-2}
1	5.35×10^{-3}	2.76×10^{-2}	1.15×10^{-2}	1.31×10^{-2}
2	5.31×10^{-3}	4.02×10^{-2}	9.82×10^{-3}	8.29×10^{-3}

From Table. 2, for each g function, we choose one case with the minimum normalized average error shown in Fig. 3. As shown in Fig. 3(a), the g_2 function is not able to give an accurate description of the icing front while the three other functions provide a satisfactory description but with some time oscillations that are compared considering the error made with the theoretical solution. In Fig. 3(b), the height of the theoretical solidification front shows $h_s \propto t^{1/2}$, but the scaling laws of other numerical functions differ from 1/2 in the beginning time. As time goes, all height evolutions gradually match well with 1/2 scaling dependence on time t. The departure for the 1/2 scaling at the beginning of the process is attributed to the oscillation of the enthalpy method formulation discussed below. Under the consideration of the lower average error and the weaker oscillation in the beginning, we regard the $g_3(p = 2)$ and $\Delta T = 2°\text{C}$ as a suitable choice for the following simulations.

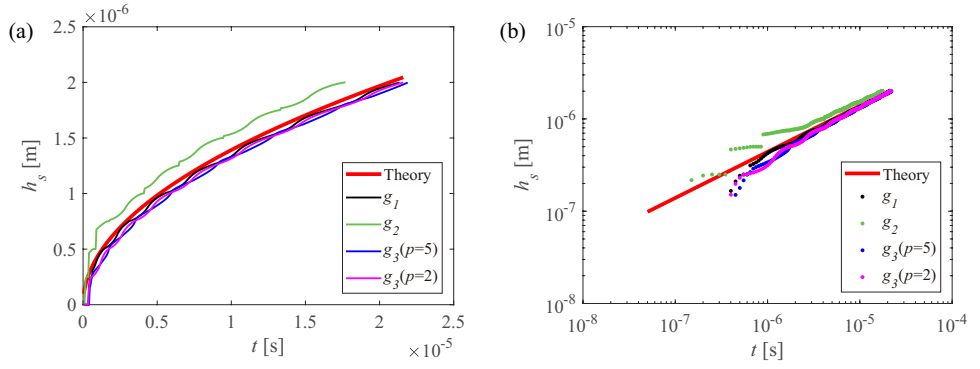

Fig. 3. Evolutions of solidification front for cases with different g functions compared to the exact solution given by relation 29. (a) a linear plot, (b) a log-log plot.

3.4. Grid and time convergence

Numerical solidification front evolutions are compared with those of theoretical solutions in Fig. 4 and Fig. 5. These two figures show the results when the height of the solidification front is smaller than $0.2h_{li}$. Considering the effect of the dimensionless grid refinement, we compare the simulations performed at the same dimensionless time step $\Delta t/t_{diff} = 1.3 \times 10^{-6}$ but with different dimensionless regular grids $\Delta/h_{li} = 4.0 \times 10^{-2}, 2.0 \times 10^{-2}, 1.0 \times 10^{-2}, 6.7 \times 10^{-3}$ to the theoretical solution shown in Fig. 4(a). We find that the grid refinement results in the convergence of the solution to the theoretical solution. The normalized maximum difference E^{Δ}_{max} is defined as

$$E^{\Delta}_{max} = \max_{k} \left(\left| h^{\Delta}_{k} - h^{TH}_{k} \right| / h^{TH}_{k} \right). \tag{34}$$

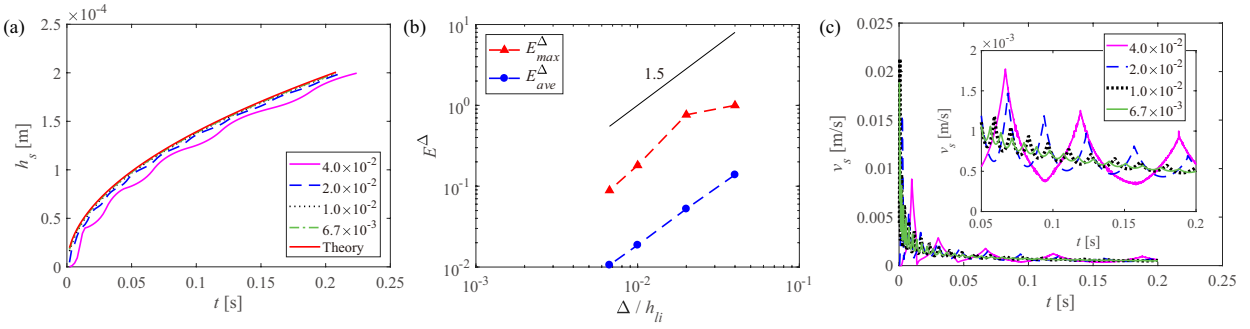

Fig. 4. Grid convergence for the evolution of the height of solidification front h_s. (a) Comparison among the numerical simulations with the same time step $\Delta t/t_{diff} = 1.3 \times 10^{-6}$ and different grid refinements Δ/h_{li} and the theoretical solution, (b) evolution of the errors E^{Δ}_{max} and E^{Δ}_{ave} as functions of the grid refinement, (c) the velocity of the solidification front $v_s = \mathrm{d}h_s(t)/\mathrm{d}t$ with the same time step $\Delta t/t_{diff} = 1.3 \times 10^{-6}$ and different grid refinements Δ/h_{li}.

The errors E^{Δ}_{max} and E^{Δ}_{ave} as functions of the grid refinement Δ/h_{li} are plotted in Fig. 4(b). This figure shows a grid convergence of order $(\Delta/h_{li})^{1.5}$ between Δ/h_{li} and $(\Delta/h_{li})^2$ for both E^{Δ}_{max} and E^{Δ}_{ave}. Decreasing the grid size can effectively decrease the difference between the theoretical result and numerical result. In addition, Fig. 4(c) shows the solidification front velocity v_s, which is calculated from $\mathrm{d}h_s/\mathrm{d}t$. Numerical oscillations observed in the velocity reported in Fig. 4(c) and Fig. 15 results from oscillations observed in the temperature evolution fields. Such oscillations have yet been identified for methods based on the enthalpy formulation and oscillations were shown to be enhanced when using coarse grids [44, 45, 46]. It is clear that reducing the grid size decreases the amplitude of these oscillations. Thus, we choose the smallest grid refinement $\Delta/h_{li} = 6.7 \times 10^{-3}$ for the following simulations. Some approaches have been proposed to reduce these oscillations for plane front [47] and their extension to general front shape (not straightforward) should provide an interesting improvement for the resolution.

Then we consider the effect of the dimensionless time step. In the Fig. 5(a), we compare the simulations performed with the same grid refinement $\Delta/h_{li} = 1.0 \times 10^{-2}$ but at different $\Delta t/t_{diff} = 1.0 \times 10^{-5}, 6.6 \times 10^{-6}, 1.3 \times 10^{-6}, 6.6 \times 10^{-7}, 1.3 \times 10^{-7}$ with the theoretical solution. All numerical results are very close

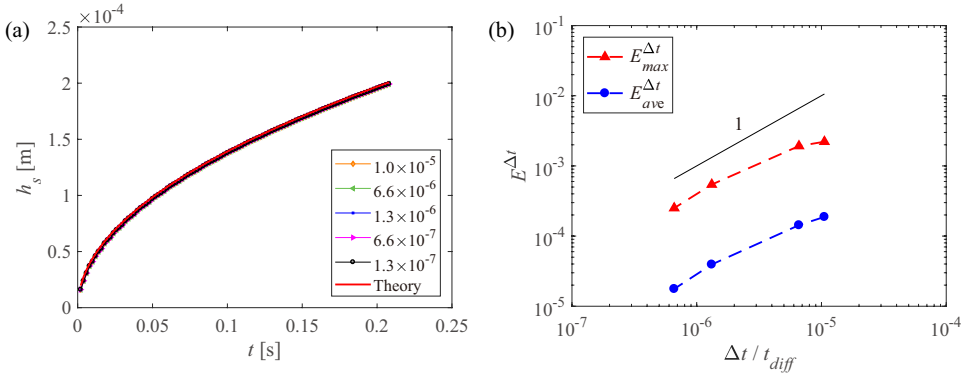

Fig. 5. Time convergence for the growth of the solidification front height h_s. (a) Comparison among the numerical simulations at the same grid refinements $\Delta/h_{li} = 1 \times 10^{-2}$ but with different time steps $\Delta t/t_{diff}$ and the theoretical solution, (b) the dependence of the errors $E^{\Delta t}_{max}$ and $E^{\Delta t}_{ave}$ on the time step.

to the exact solution but there is not a clear dependence between h and the time step. So we use the the normalized maximum difference $E^{\Delta t}_{max}$ and the normalized mean difference $E^{\Delta t}_{ave}$ from the solution of reference obtained for the smallest time step considered $\Delta t/t_{diff} = 1.3 \times 10^{-7}$:

$$E^{\Delta t}_{max} = \max_k \left(\left| h^{\Delta t}_k - h^{\Delta t/t_{diff}=1.3\times10^{-7}}_k \right| / h^{\Delta t/t_{diff}=1.3\times10^{-7}}_k \right), \tag{35}$$

$$E^{\Delta t}_{ave} = \frac{1}{k}\sum_k \left(\left| h^{\Delta t}_k - h^{\Delta t/t_{diff}=1.3\times10^{-7}}_k \right| / h^{\Delta t/t_{diff}=1.3\times10^{-7}}_k \right). \tag{36}$$

The errors $E^{\Delta t}_{max}$ and $E^{\Delta t}_{ave}$ as functions of the time step $\Delta t/t_{diff}$ are reported in Fig. 5(b). This figure shows a time step dependence of first order $(\Delta t/t_{diff})^1$ for both $E^{\Delta t}_{max}$ and $E^{\Delta t}_{ave}$. In the range of our investigation, the errors caused by the time step dependence is much smaller than that caused by the grid resolution. The change of the error caused by different time steps is much smaller, so the error is mainly determined by the grid refinement. Combining the consideration of the calculation efficiency and accuracy, we choose the time step $\Delta t/t_{diff} = 1.3 \times 10^{-6}$ for the following simulations.

For the simulations, the volume of the liquid is limited, so there will be a moment when all of the liquid freezes to the solid. It causes the difference compared with the theory based on an infinite volume of liquid. In most realistic situations, the volume of the liquid is limited, thus our simulations give a more complete picture on the icing process of a finite volume liquid. And the mass conversation law can be used to check the accuracy of the simulations.

We calculate the grid and time convergences of the final height of the solidification front h_{se}. The parameters are the same as those of the Fig. 4 and the Fig. 5. The corresponding errors E^{Δ}_{se} and $E^{\Delta t}_{se}$ are defined as

$$E^{\Delta}_{se} = \left| h^{\Delta}_{se} - h^{TH}_{se} \right| / h^{TH}_{se}, \tag{37}$$

$$E^{\Delta t}_{se} = \left| h^{\Delta t}_{se} - h^{TH}_{se} \right| / h^{TH}_{se}. \tag{38}$$

All of the studied E^{Δ}_{se} and $E^{\Delta t}_{se}$ reported in Fig. 6 (b,d) are smaller than 3.0×10^{-3}, suggesting that the

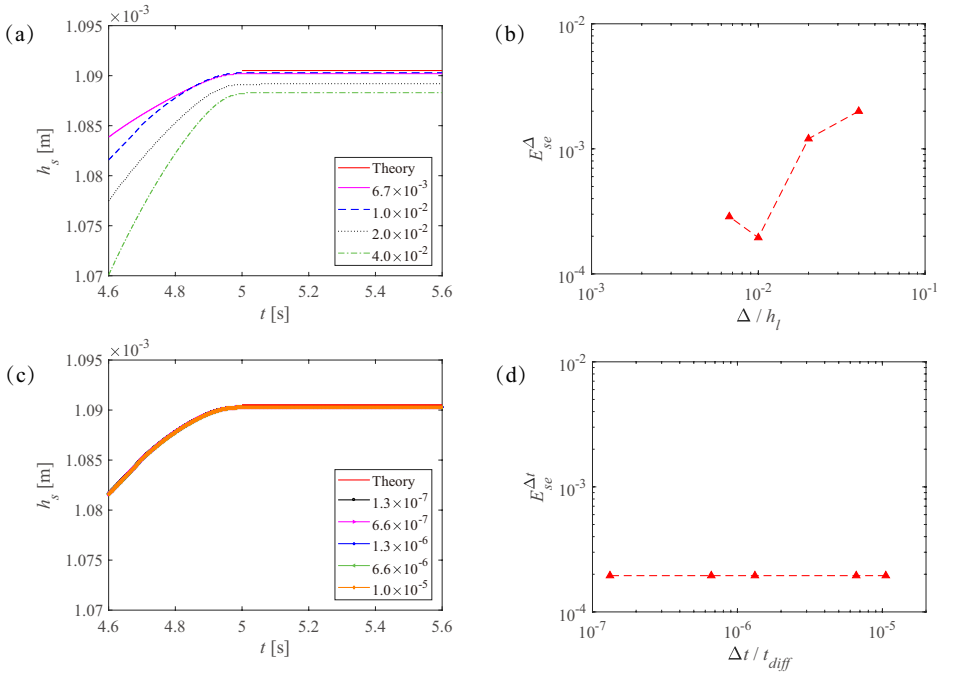

Fig. 6. Grid and time convergences of the final height of the solidification front h_{se}. (a) The final evolution of the height of the ice with different grid refinements Δ/h_{li}, (b) the dependence of the error of the final height of the ice E_{se}^{Δ} on the grid refinement Δ/h_{li} with the same time step $\Delta t/t_{diff} = 1.3 \times 10^{-6}$, (c) the final evolution of the height on different time steps $\Delta t/t_{diff}$, (d) the dependence of the error of the final height $E_{se}^{\Delta t}$ on the time step $\Delta t/t_{diff}$ at the same grid refinements $\Delta/h_{li} = 1 \times 10^{-2}$.

icing simulations of liquid films conform the mass conservation law. In the Fig. 6 (a,b), the grid size has an important influence of the final height of solid and E_{se}^{Δ} decreases with the Δ/h_{li} until 1.0×10^{-2}. In the Fig. 6 (c,d), $E_{se}^{\Delta t}$ doesn't change with the $\Delta t/t_{diff}$.

3.5. The effect of different parameters on the icing processes

In order to well control and understand the icing processes, we need to investigate the effect of different variables on the icing process. Firstly, we focus on the density difference due to solidification. For most materials, the densities are different between the liquid phase and solid phase. However, many numerical studies ignored the density difference between the water and ice as the density contrast is small [6, 48, 49, 50, 51]. However, we find that even the small density difference results in notable effects. Based on the time and grid tests presented above, the simulations are conducted with $\Delta/h_{li} = 6.7 \times 10^{-3}$ and $\Delta t/t_{diff} = 1.3 \times 10^{-6}$. In Fig. 7(a), the evolution of the solid height h_s are shown as the solid lines and the liquid height h_l are shown as the dashed lines at varying different density ratios $\rho_s/\rho_l = 0.6, 0.8, 0.917, 1$. Keep the density of the liquid is a constant and change the density of the solid. At the freezing time t_f when $h_l = h_s$, all of the liquid freezes to the solid. We find that even if the initial liquid heights are the same, the freezing times t_f have a large difference due to the density difference. As the density ratio decreases, the freezing time increases. There may be two reasons for that dependence, firstly the smaller density ratio means the liquid occurs a larger expansion and the final height of the solid h_{se} is larger; secondly, from the Fig. 7(a) we

observe that the velocity of the solid front v_s at the same height decreases with the decreasing density ratio. For the same height of the solid, the smaller density ratio means that the mass of liquid freezing to the solid is less. At this time, even the temperature gradient in the solid is the same, more mass of the liquid left to be cold for the material with the smaller density ratio. Consequently, the freezing time becomes larger for smaller density ratio case. We know that the initial numerical result fits well with the theoretical solution. And the theoretical velocity of the front is $\delta(\alpha_s/t)^{1/2}$, so we compute the constant δ as a function of the density ratio in Fig. 7(b). As shown in Fig. 7(b), when the density ratio decreases, the constant δ becomes smaller and the velocity of the front is smaller. The theoretical solution also validates this conclusion. In Fig. 7(c), we use the mass conservation law to calculate the theoretical result of the final height of the solid as a function of the density ratio, $h_{se} = h_{li}/(\rho_s/\rho_l)$. The red line shows the theoretical result and the blue solid circles are numerical results. The errors of the final height of solid E_{se} of Fig. 7(c) are smaller than 5×10^{-4}. The perfect agreement between the numerical results and the theoretical solution indicates that our simulations satisfy the mass conservation law.

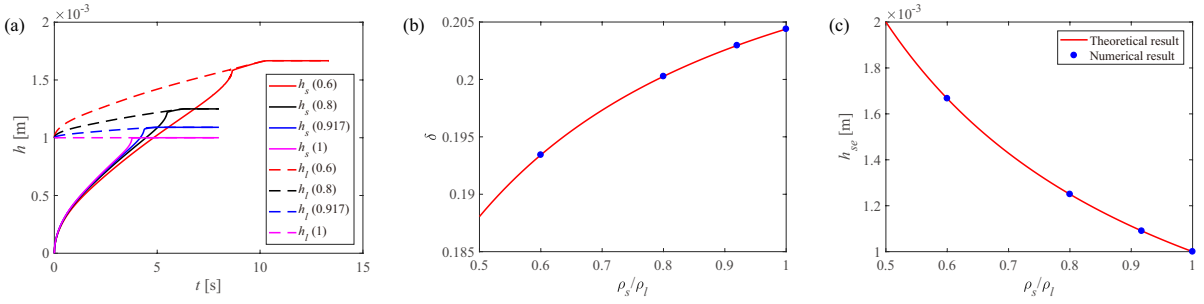

Fig. 7. The dependence of liquid height h_l and solid height h_s on the density ratio ρ_s/ρ_l. (a) The evolution of the solid height h_s shown as the solid lines and the liquid height h_l shown as the dashed lines at varying ρ_s/ρ_l=0.6, 0.8, 0.917, 1; (b) the constant in the theoretical velocity of the solidification front as a function of the density ratio; (c) after all liquid freezes to solid, the final solid height h_{se} varies with the density ratio. The red line shows the theoretical result and the blue solid circles are the numerical results.

Then we investigate the effect of the initial conditions. In Fig. 8(a), we only change the initial temperature and other parameters are kept the same as before mentioned. The Stefan number Ste is used to describe the ratio of sensible heat to latent heat. We use the blue dot-dash line as a reference with the initial temperatures of the liquid and the gas are $T_{gi} = T_{li} = T_i = 20°\text{C}$, the temperature of the wall is $T_w = -20°\text{C}$ and the Stefan number is $Ste = 0.12$. When we decrease the initial temperature of the liquid and the gas to 5°C, we find the freezing process becomes quicker as shown in the red dashed line at the same $Ste = 0.12$. In addition, if we keep the initial temperature of the liquid and that of gas are the same and increase the temperature of the wall to −5°C and the corresponding Ste becomes 0.04, as expected, the freezing process becomes much slower. So it means by decreasing the Ste, the freezing process can be slowed down. The solid lines are theoretical lines, which have the same initial conditions as the numerical lines with the same color. The lower temperature of the wall results in a larger temperature gradient in the solid, consequently the freezing process is speeded up. For a lower temperature of the liquid, the sensible heat of the liquid and

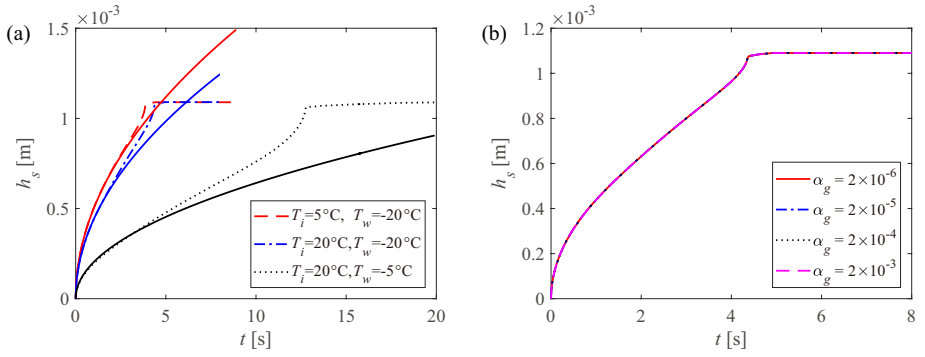

Fig. 8. The effect of the initial condition. (a) The evolution of the solid height at different initial temperatures. The solid lines show the theoretical results and other lines with the same color show the corresponding numerical results. (b) The evolution of the solid height at different thermal diffusivities of the gas.

gas is much smaller, thus the solidification process is much faster. We find that even for different initial conditions, the numerical solution still fits well with the theoretical solution in the beginning, and the final height of the solid conforms the mass conservation law.

In the Fig. 8(b), we study the effect of the thermal diffusivity of the gas $\alpha_g = \lambda_g/(\rho_g C_{pg})$ on icing front evolution. The thermal diffusivity of the liquid is $\alpha_l = 1.32 \times 10^{-7}$ m^2/s. We keep the ρ_g and C_{pg} to be constants and only vary the heat conductivity of the gas λ_g to be $\alpha_g = 2\times10^{-3}, 2\times10^{-4}, 2\times10^{-5}, 2\times10^{-6}$ m^2/s. Because the south wall is the only cold source, and the gas and the cold source are separated by the liquid and the solid, so the gas is only cooled by the liquid. All the α_g studied here are much larger than the α_l, so the temperature of the gas quickly becomes a constant as the same as that of the liquid front (seen in the Fig. 13 (d)). And since $\rho_g C_{pg}$ is small, the reduction of gas temperature doesn't release a lot of energy. Thus the solidification front evolutions are nearly the same for the considered α_g, as shown in the Fig. 8(b).

In the Fig. 9, we study the effect of the initial height of the liquid h_{li}/h_d on icing front evolution. h_d is the height of the numerical domain. In the Fig. 9 (a), solid lines show the numerical results with different initial liquid heights and dashed lines show the theoretical solutions. The same color represents the same initial height. No matter what the initial height of the liquid is, the initial solidification front matches well with the theoretical solution. We define the $h_m = 0.5h_{se}$ and the t_m the corresponding time when the solidification front reaches to h_m. Using the h_s/h_m and t/t_m to normalize the height evolution, all of the data collapse to the theoretical line. Thus, the h_{li}/h_d doesn't change the initial non-dimensional solidification evolution of the liquid film, which only conforms the theoretical law.

4. Freezing liquid film in a 2D container

We present now a 2D test case in order to validate the dilatation process in 2D. For that purpose, we simulate the freezing of a liquid film in a cold container. The boundary conditions are defined as follows for the velocity (resp. temperature): (a) for the north wall, an outlet (resp. adiabatic) condition; (b) for

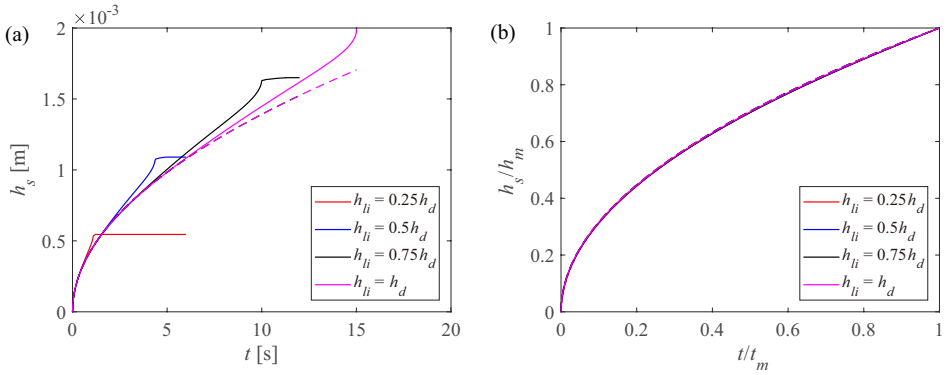

Fig. 9. The effect of the initial height of liquid. (a) The evolution of the solidification front with different initial liquid height h_{li}/h_d, (b) the initial stage of the solidification front evolution.

the east wall, a symmetry (resp. symmetry) condition; (c) for the south and west walls, no slip (resp. imposed cold temperature) condition. The imposed temperatures of the walls are $T_w = -20°\text{C}$, and the initial temperatures of the liquid and that of the gas are $T_{li} = T_{gi} = 20°\text{C}$. In Fig. 10, the density ratios of the solid phase to liquid phase are 1 and 0.917 respectively. The solidification fronts are marked by white lines, and the liquid-gas interfaces are marked by black lines.

In order to quantitatively record the freezing process, we calculate the height evolution h_{west} and h_{south} from the cold wall of two special points, which are marked in Fig. 10(b). The evolutions of h_{west} and h_{south} are plotted in Fig. 11. For cases with the density ratio 1, there is no dilatation for the freezing liquid and the two height evolutions of h_{west} and h_{south} are the same. However, if the density ratio is 0.917, the two height evolutions differs because of the dilatation. Because of non deformable west, south and east boundaries, the dilatation is only possible in the vertical direction. Thus, the liquid is pushed upwards, and the final solidification front becomes curved. As a consequence of a final smaller ice thickness, the case without dilatation has a higher freezing rate and a shorter frozen time.

We also calculate the final area of ice, which is shown in Table. 3. A_n and A_t are the numerical value and the theoretical value respectively. $E = |A_n - A_t|/A_t$ is the error between the numerical value and the theoretical value. We find both cases with different density ratios fit well with mass conservation.

Table 3. The final area of the frozen liquid film.

ρ_s/ρ_l	A_n [mm^2]	A_t [mm^2]	$E = \lvert A_n - A_t\rvert/A_t$
1	1.0000	1.0000	1×10^{-13} %
0.917	1.0903	1.0905	0.02 %

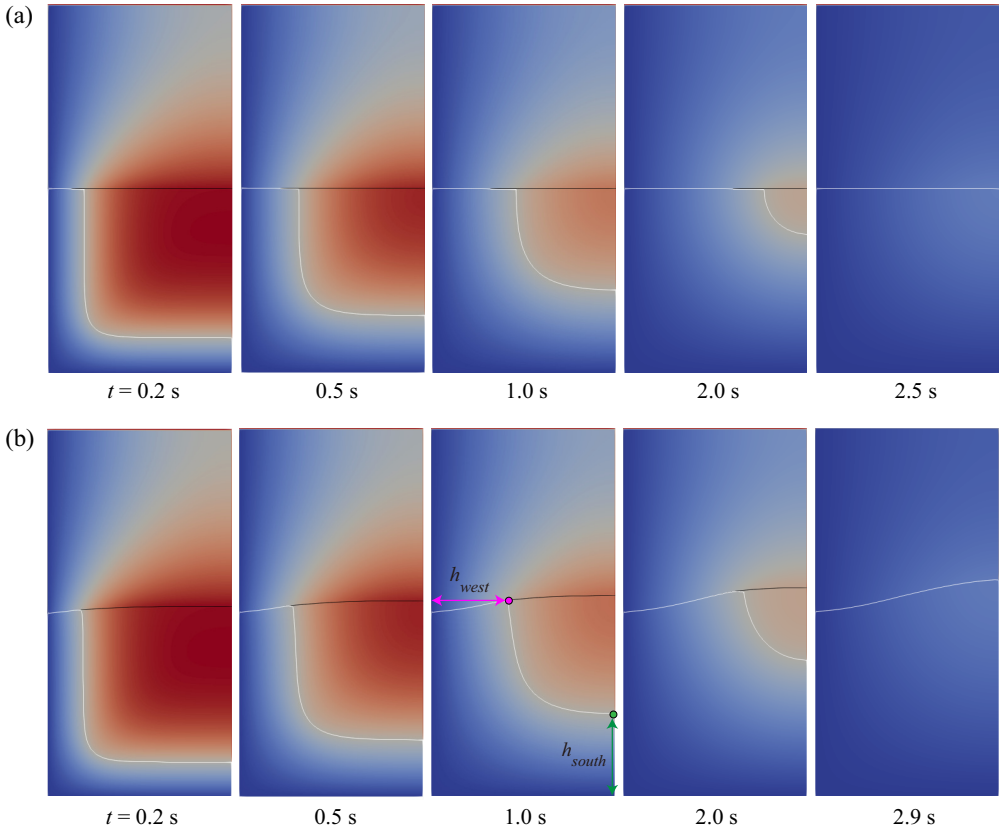

Fig. 10. Liquid film is cooled down by west and south walls. The solidification fronts are marked by white lines, and the liquid-gas interfaces are marked by black lines. The height evolutions of two special points h_{west} and h_{south} are marked in Fig. 10(b). In (a) and (b), the density ratios of the solid phase to liquid phase are 1 and 0.917 respectively.

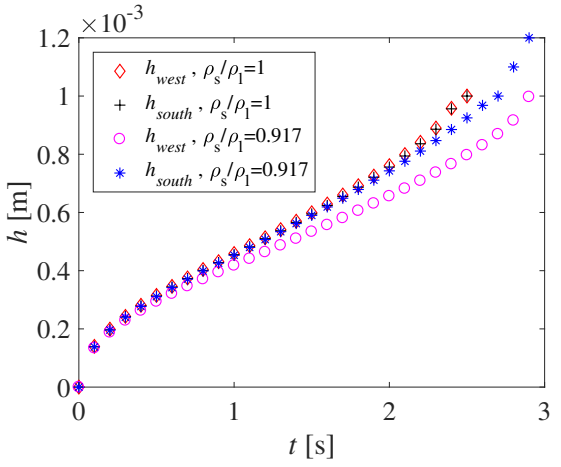

Fig. 11. The height evolutions of h_{west} and h_{south} for cases with different density ratios, such as $\rho_s/\rho_l = 1$ and $\rho_s/\rho_l = 0.917$.

5. Drop without surface tension and gravity icing on a horizontal cold surface

As we have validated the accuracy of the VoF-IBM method for simulation of 1D and 2D freezing liquid film, we now apply it to simulate freezing axisymmetric drop. In experiments, it's difficult to precisely identify the freezing front inside the drop. Through our simulations, the evolution of the solidification front height, the shape of the solidification front, the freezing rate, the temperature, velocity and pressure distributions inside the drop can be fully accessed. Through the comparison between the liquid film and drops with different geometries, we can clearly understand the effect of the geometry of drop and shape of the solidification front on freezing process.

The parameters in the numerical domain are as follows: the north wall is at the wall condition and adiabatic; the west wall is at the wall condition and at the constant temperature; the south wall is the symmetry axis and the east wall is the outlet and adiabatic. In order to clearly show the process, we add the reflection of the symmetry axis and rotate the figure 90 degrees in the counterclockwise direction. In the Fig. 12, we show the freezing process of a drop on a solid wall. The blue area is the gas. The black lines cover the interface of ice, and the rest part is the liquid. The shape of the drop is a spherical cap. Some important parameters are shown in the Fig. 12, such as θ the contact angle of the drop, γ the angle in the solid area between the solid-liquid interface and the solid-gas interface, α the tip angle of the final solid drop, h_{li} the initial height of the top of the drop, and $h_s(t)$ the height of the solidification front in the axis. As explained in section 2.3.2, there is no special angle imposed at the triple line, thus thermal properties (i.e. the heat flux) control the angle γ made between the freezing front and the drop surface. For a nearly adiabatic condition of gas, the angle γ is 90° [3].

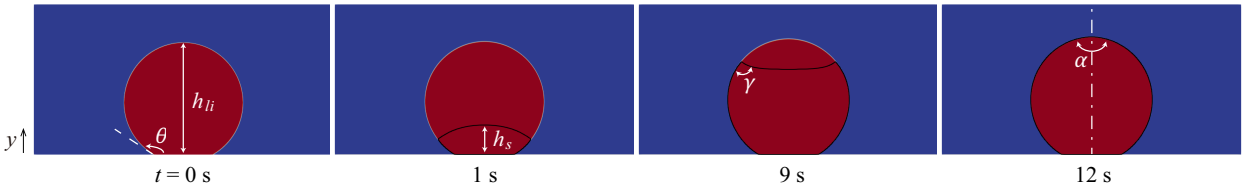

Fig. 12. The configuration of a freezing drop on a cold solid wall at different moments t. The definitions of parameters $\theta, h_{li}, h_s, \gamma, \alpha$ are also shown in the figure. The blue area is gas; the black lines cover the interface of solid and the rest part is liquid.

5.1. Comparison of the freezing process between a flat liquid film and a drop.

Besides the physical properties of the liquid, the geometry of the liquid also affects the freezing process. In the following, we compare the freezing process between a flat liquid film and a drop.

In the Fig. 13 and Fig. 14, we quantitatively analyze the temperature, velocity and pressure distributions and interfaces within the liquid film and drop respectively. In the Fig. 13 (a), we plot the height evolution of two interfaces. The red line shows the theoretical height of the solid interface; the blue line shows the numerical height of the solid interface; the black line shows the numerical height of the liquid interface; and

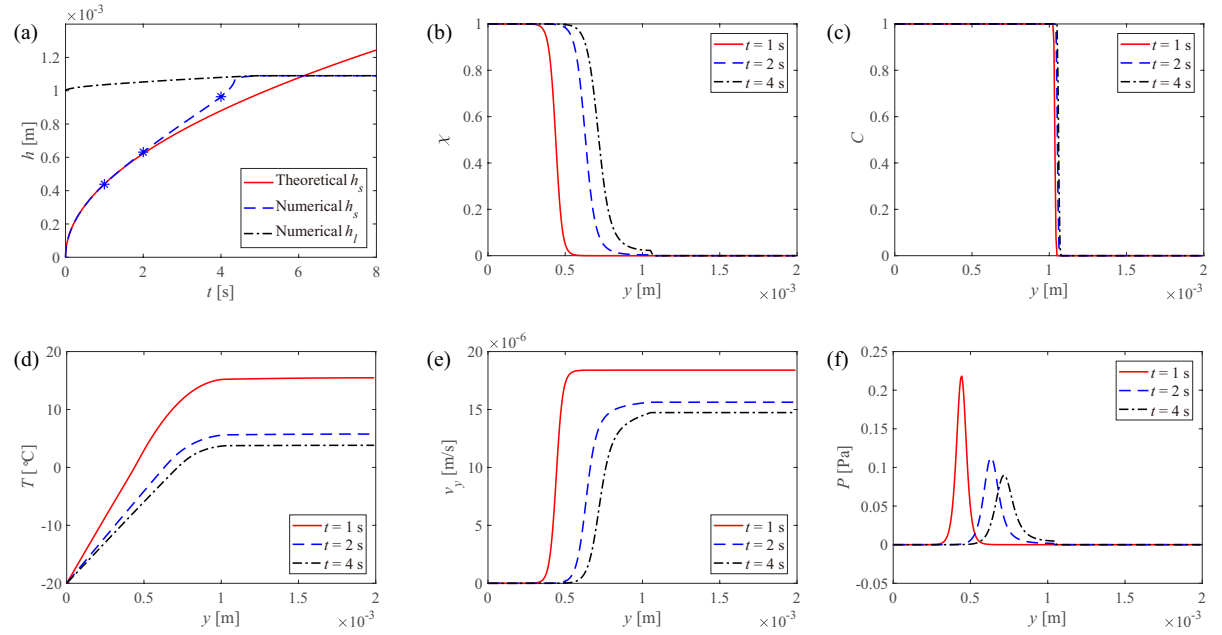

Fig. 13. The inner parameter distributions of the liquid film along the symmetry axis at different moments. (a) The evolution of the height of the gas-liquid and liquid-solid interfaces, blue stars show three studied moments, (b) the distribution of the χ function at different moments, (c) the distribution of the C function at different moments, (d) the distribution of the temperature at different moments, (e) the distribution of the velocity in the y direction at different moments, (f) the distribution of the pressure at different moments.

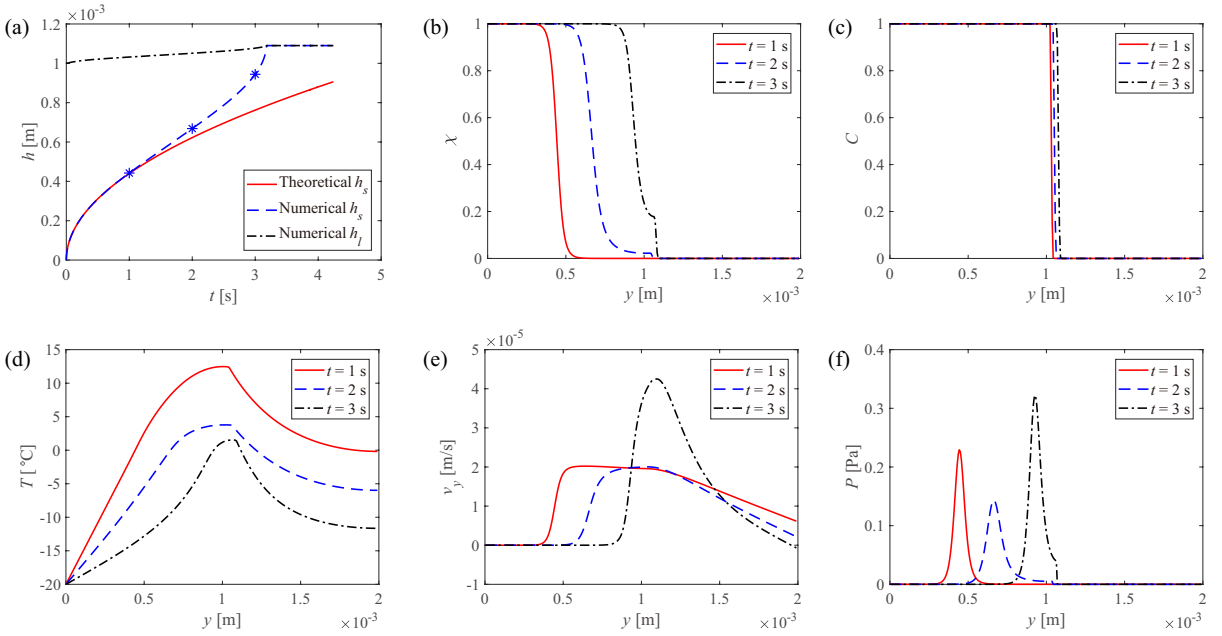

Fig. 14. The inner parameter distributions of the drop along the symmetry axis at different moments. (a) The evolution of the height of the gas-liquid and liquid-solid interfaces, blue stars show three studied moments, (b) the distribution of the χ function at different moments, (c) the distribution of the C function at different moments, (d) the distribution of the temperature at different moments, (e) the distribution of the velocity in the y direction at different moments, (f) the distribution of the pressure at different moments.

three blue stars mark following studied moments. In the Fig. 13 (b), the χ function distribution at three moments are shown. In the solid phase $\chi = 1$; in the liquid and gas phase $\chi = 0$; in the transition stage, χ function is used to smooth the sharp changes between different phases; and $\chi = 0.5$ helps to visualize the position of the solid interface. In the Fig. 13 (c), the C function distributions at three moments are shown. In the solid and liquid phase $C = 1$; in the gas phase $C = 0$; the transition range is linear; and $C = 0.5$ is used as a criterion used to obtain the position of the gas interface. The temperature distributions are shown in the Fig. 13 (d). It has a large temperature gradient in the solid and liquid phase, but in the gas phase, the temperature gradient is very small and the temperature decreases over time. The velocity distributions are shown in the Fig. 13 (e). The velocity in the solid phase is zero; the velocity has a smooth increase in the transition stage, and the velocities of the liquid phase and gas phase are the same thanks to mass conservation. The maximum velocity decreases with time. The pressure distribution is shown in the Fig. 13 (f). It has a sharp peak in the IBM transition region between the solid and liquid phases.

We compare the Fig. 13 and Fig. 14 to get the difference between the liquid film and drop. In the Fig. 14 (a), even if the initial liquid height is the same as that of liquid film, the freezing time of the drop is smaller. In the Fig. 14 (d), the temperature profile shows that the temperature decreases in the gas phase because the gas can be directly cooled by the cold substrate. In the Fig. 14 (e), the velocity in the solid phase is zero; it increases in the solid-liquid transition phase; the velocity of the liquid phase is nearly uniform; and it decreases in the gas phase because of mass conservation is spherical geometry. Interestingly we observe that the maximum velocity has a rapid increase in the end of the frozen process. In the Fig. 14 (f), we find a similar pressure distribution with a peak in the IBM transition region between the solid and liquid phase. A pressure at the ice front appears because the liquid is pushed by the ice front. The velocity ranges from zero in ice to the velocity in liquid due to the dilatation, which induces a pressure gradient in the resolution.

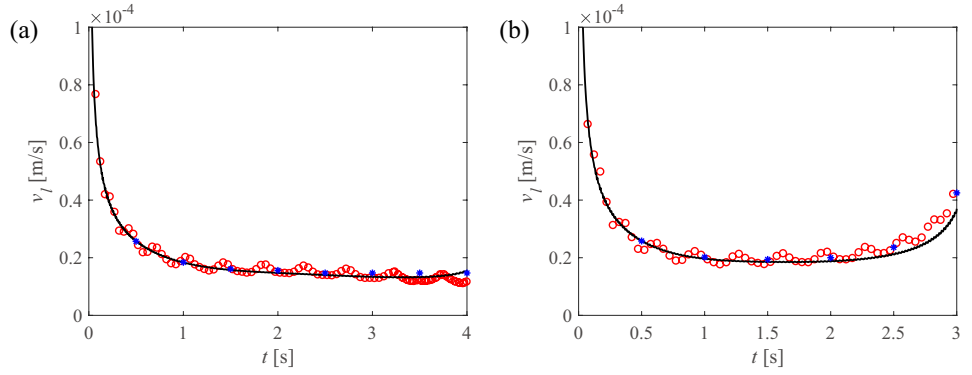

Fig. 15. Comparison among three velocities along the symmetry axis. Black lines represent the result of the Eqn. 25 $v_l = \frac{\mathrm{d}h_s}{\mathrm{d}t}\left(1 - \frac{\rho_s}{\rho_l}\right)$, red circles show the result of $v_l = \frac{\mathrm{d}h_l}{\mathrm{d}t}$, and blue stars show the maximum velocity along the symmetry axis. (a) and (b) show results of the liquid film and drop respectively.

We report in Fig. 15 the evolution of the velocity of the liquid v_l along the symmetry axis. Black lines show the result of the Eqn. 25 $v_l = \frac{\mathrm{d}h_s}{\mathrm{d}t}\left(1 - \frac{\rho_s}{\rho_l}\right)$ where h_s is determined at the position with the $\chi = 0.5$;

red circles show the velocity of the liquid front $v_l = \frac{\mathrm{d}h_l}{\mathrm{d}t}$ where h_l is determined at the position with $C = 0.5$; and blue stars show the maximum velocity v_{max} along the symmetric axis. The Eqn. 25 considers the expansion of the solidification and part of liquid freezes to the solid. As shown three velocities follow very close evolutions. This result clearly demonstrates the connection between the drop deformation at the tip and the liquid displacement induced by the ice formation. In particular, as shown in the Fig. 15(b), the liquid velocity in the drop becomes faster in the end, which results from the acceleration of the frozen process, the liquid volume to be iced decreasing faster than the heat flux from the cold source.

We now consider the effect of the density ratio on the solidification of both the liquid film and the drop. In Fig. 16, we compare the evolution of the solidification front for different density ratio. The solid lines plot the results of liquid films and the dashed lines plot the results of drops. The same color means the same density ratio. Increasing the density ratio, increases the dilatation and thus the final height of the solid. As outlined for the larger density ratio, the difference of the final height of the solid is slightly larger for the liquid film. The explanation is that for the liquid film the expansion is only in the vertical direction while for the 2D drop expansion can also occur along the side directions. Though the final height of the solid is comparable, the freezing rate for the drops is quicker and the corresponding freezing time for the drops is clearly smaller.

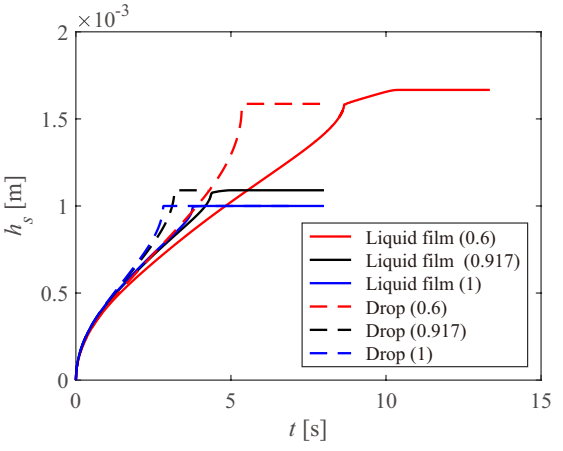

Fig. 16. Comparison of the effect of the density ratio ρ_s/ρ_l on the solidification process between the liquid film and drop. The evolutions of the solid height of the liquid film and the drop, respectively shown as the solid lines and dashed lines. The same color represents the same density ratio.

5.2. Effect of the contact angle on drop icing

When a drop spreads on the substrates with different wettabilities, even the volume of the drop is the same, but the contact angle plays important roles on the shape of the drop on the surface. In the following, we study the effect of the contact angle on the freezing process of a drop.

We choose five drops with different contact angles, i.e. $\theta = 30°, 60°, 90°, 120°, 150°$. The volume of the drop is kept to be the same $2.09 \times 10^{-9}\mathrm{m}^3$ and the shape of the drop is a spherical cap. In Fig. 18(a), from

the left to right, the contact angles are $\theta = 30°, 90°, 150°$. We show the temperature distributions at the same moment $t = 0.5$s. The blue lines show the interface of solid and the black lines show the gas-liquid interface. It shows that the shapes of the solidification fronts for different contact angles are totally different. In the first and the second cases, the freezing fronts have concave shapes and the third one has a convex shape. Fig. 18(b) shows that the freezing time increases with the contact angle for drops with the same initial volume, which is also observed in the experiment [8]. One main reason is that the final height of the solid increases with the increasing contact angle. Another reason is that the freezing rate is also different for different contact angles. Fig. 18(c) shows that at the same height of the solidification front, the freezing rate is smaller for the larger contact angle case. The evolution of the freezing time t_f with the contact angle θ is reported in Fig. 18(d). t_f is compared with the diffusion time $t_d = h_{li}^2/\alpha_l$, the blue circle lines show the diffusion time and the red triangle lines show the freezing time. Fig. 18(d) shows that the freezing time is smaller than the diffusion time. As the solidification evolves, the front is becoming more and more concave, as a consequence the liquid can be cooled not only by the vertical direction but also by the side direction, which helps to speed up the freezing process. We also investigate the tip angle α of the final frozen drops with different contact angles, which are shown in Table 4. All tip angles are smaller than 180° because the solidification of liquid push the left liquid to move upwards to create a new shape of the drop [3]. However the values in Table 4 are significantly larger than the values ranging from 139 to 147° reported by the experiments of [3] when varying the contact angle. This point will be discussed in more details in the next section.

Table 4. The tip angle α of frozen drops

Contact angle θ [°]	30	60	90	120	150
Tip angle α [°]	173	169	170	164	162

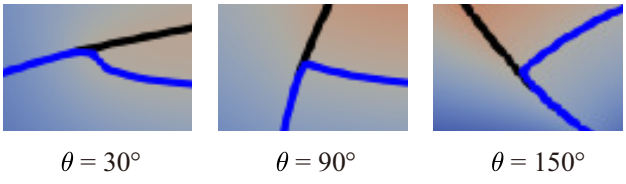

Fig. 17. The front-to-interface angle γ for different freezing drops at $t = 0.5$ s. The black lines represent the interfaces between the gas and liquid. The blue lines show the interfaces of the solid phase.

In addition, the front-to-interface angle γ is investigated as shown in Fig. 17 at the same freezing time $t = 0.5$ s. Three contact angle are reported 30^o, 90^o and 150^o. The black lines represent the interfaces between the gas and liquid. The blue lines show the interfaces of the solid phase. As shown, even if the shapes of the solidification fronts are different, they are nearly perpendicular to the droplet interfaces, which means a front-to-interface angle $\gamma \approx 90°$. Such result is also reported in the experiments [3], as a consequence of the poor conductivity of the gas. The freezing front at T_m is an isotherm line, which is perpendicular to

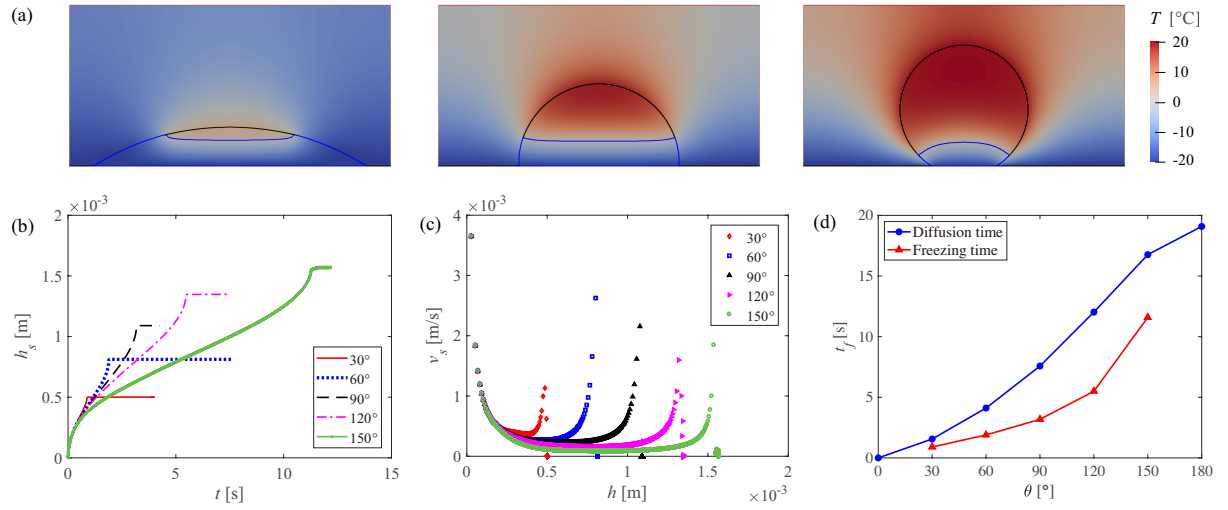

Fig. 18. The effect of the contact angle on the freezing process. (a) At the same moment, the temperature distribution for drops with the same volume and different contact angles from left to right $\theta = 30°, 90°, 150°$, (b) the evolutions of the solid height at the axis line for cases with different contact angles, (c) the dependence of the solid front velocity at the axis line on the position of the solid front for cases with different contact angles, (d) comparison between the dependence of the diffusion time and the numerical freezing time on the contact angles.

the droplet interface because there is a small heat flux cross the solid-gas boundary.

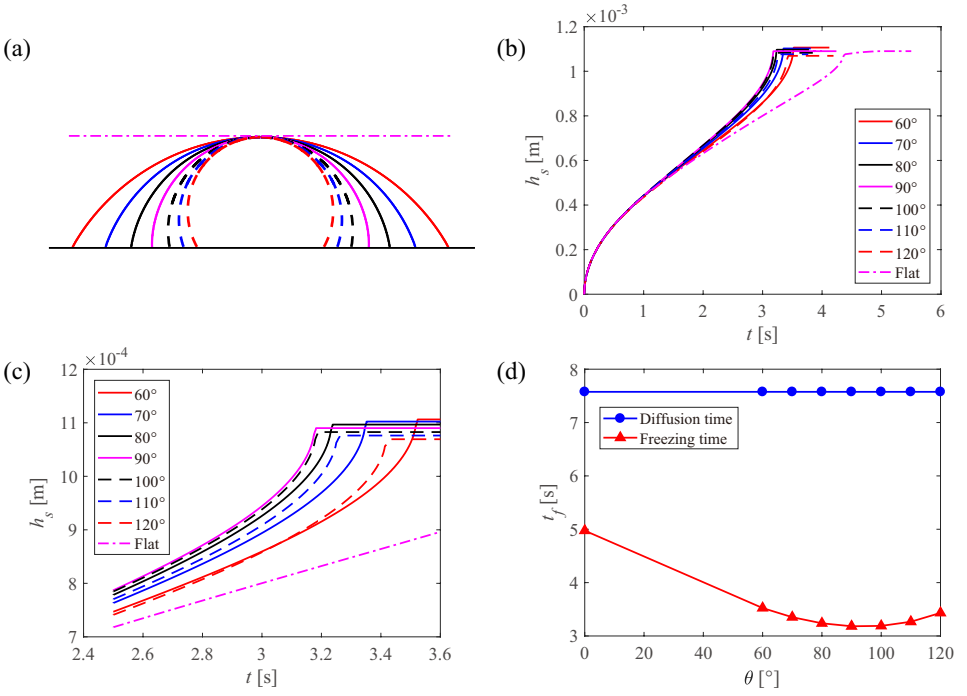

Fig. 19. The effect of the contact angle on the solidification process of drops with the same initial liquid height. (a) The profile of the initial liquid film and drops with different contact angles, (b) the evolution of solidification front, (c) partial enlargement of the end of the solidification process shown in (b), (d) comparison between the dependence of the diffusion time and the numerical freezing time t_f on the contact angles.

The biggest reason of different freezing times in the Fig. 18 is caused by the difference of the liquid height. Thus we now compare the freezing time of the liquid film and drops with the same initial liquid height and different contact angles shown in the Fig. 19 (a). In the Fig. 19 (b), we find that the freezing time of drops are much smaller than that of the liquid film. If we compare the partial enlargement of final solidification process in the Fig. 19 (c,d), an interesting phenomenon is found. The condition of liquid film can be regarded as the drop with $\theta = 0°$. When the contact angle is smaller than 90°, the freezing time t_f decreases with the increasing contact angle, but once the contact angle is larger than 90°, the t_f increases with the contact angle. Thus for drops with the same initial liquid height, the drop with the contact angle 90° freezes the fastest and the liquid film freezes the slowest. For drops with contact angle smaller than 90°, the icing front area is smaller than the bottom area, so the solidification front is always concave. For the front at the central axis, it is not only cooled by the vertical direction but also cooled by the horizontal direction. As the contact angle increases, the horizontal temperature gradient becomes larger for the same height, so the freezing times decreases. But once the contact angle is larger than 90°, the front at the central axis must be warmed by the horizontal direction in the beginning, so it will slow down the solidification rate. As the contact angle increases, this slow freezing process lasts longer, so the total freezing time increases with the contact angle. For the liquid film, the front is only cooled by the vertical direction, and there is no help of the horizontal direction, so it needs the longest time to be frozen.

6. Drop with surface tension and gravity icing on a horizontal cold surface

In the former section, we have investigated the effects of different parameters on the freezing process, such as the density ratio, the initial temperature of liquid and wall, the heat conductivity of gas, the contact angle of the drop, the initial volume of the drop and the geometry of the drop. In the reality, two other important parameters are also expected to affect the freezing process, such as the gravity and the surface tension, because the combination of these two forces controls the shape of the liquid part of the drop. In the following, we firstly study the effect of surface tension on the freezing drop, then we discuss the magnitude of the spurious currents that develop at the gas/liquid interface and finally we compare the simulation to experiment.

6.1. The effect of the surface tension and the gravity

In the former sections, the change of the drop shape is mainly determined by the expansion of volume caused by the liquid solidification. But if we consider the real condition, as the liquid is pushed by the ice expansion, the shape of the liquid part is controlled by forces balance at the interface where the surface tension tends to minimize the area of the liquid interface while gravity tends to spread the liquid. In the simulations, we consider the water/air system so the surface tension between the air and water is 0.072 N/m and the gravity is 9.81 m/s^2. The initial shape of the drop is a spherical cap with radius $R = 1$ mm and contact angle $\theta = 90°$ so that the initial drop height is $h_{li} = R = 1 \times 10^{-3}$m. The corresponding

Bond number $Bo = \rho g d_{eq}^2/\sigma = 0.34$ (where d_{eq} is the equivalent diameter). Bo has been selected less than unity resulting in an initial spherical drop in order to make easier the discussion on the effect of the surface tension on the icing process. In addition, considering the maximum value of the liquid velocity $v_l \approx 10^{-3}$m/s expected inside the drop (see Fig. 15), the Weber number $We = \rho v_l^2 d_{eq}/\sigma \approx 10^{-5}$ and the capillary number $Ca = \mu v_l/\sigma \approx 10^{-5}$ are both much smaller than unity indicating that the velocity field is not expected to induce interface deformation.

We compare two simulations in Fig. 20 (a,b). The solid lines show the profile of the drop and the dashed lines show the solidification front at different times. In the Fig. 20 (a), gravity and surface tension are not considered so the change of the drop shape is only caused by the expansion due to the solidification. The drop shape doesn't change a lot and the resulting tip angle remains close to the initial shape. In the simulations reported in Fig. 20 (b), surface tension and gravity are considered. As clearly observed, the effect of surface tension becomes more and more pronounced during the solidification as the liquid volume is reduced resulting in a larger change of the drop shape and a sharper tip angle. We also compare the evolution of the solidification front for these two simulations in Fig. 20 (c). We find that the evolution of the front propagation is very close up to end of the icing corresponding to the tip formation. The freezing time of a drop with surface tension is larger because we get a larger final height of the iced drop. This clearly indicates that surface tension effects are controlling the drop shape evolution and tip formation. The explanation is as follows. The characteristic capillary time $\tau_{cap} = \sqrt{\rho R^3/\sigma} \approx 4 \times 10^{-3}$s is much smaller than the icing time $t_f \approx 3$s. Thus, when the ice front propagates the capillary effect has time to adjust the shape of the remaining volume of liquid to a spherical cap. This changes the drop shape compared to the initial spherical cap as shown in Fig. 20 (b).

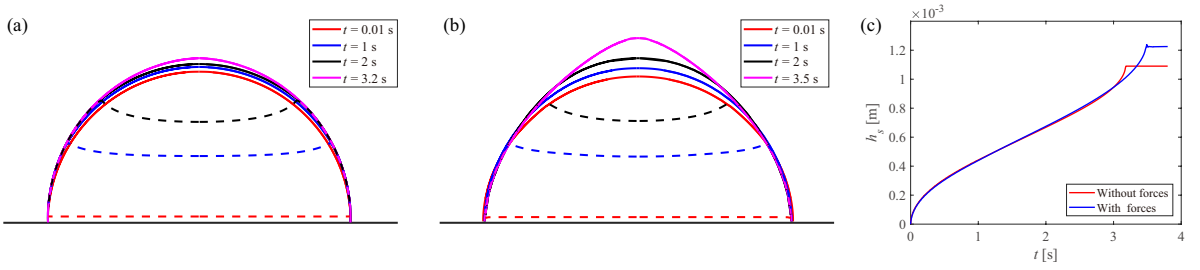

Fig. 20. The effect of surface tension and gravity on the solidification process. (a) The freezing process of drops without surface tension and gravity, (b) the freezing process of drops with surface tension and gravity, (c) the evolution of the solidification front: in red simulation without surface tension and gravity, in blue

We consider the mass conservation for the two cases. The initial shape of the drop being a spherical cup with radius $R = 1$ mm and $\theta = 90°$, the initial volume of water is 2.0944 μL and the final volume of the frozen drop V_t is 2.2840 μL. For the case without surface tension and gravity, the final volume of the frozen drop is $V_t = 2.2826$ μL and that of case without surface tension and gravity is $V_t = 2.2575$ μL. The volume error E_V is defined as $|V_f - V_t|/V_t$ is found to be smaller than 1.5% for the two cases.

In order to compare the freezing process between a flat liquid film and drops, we set the initial height

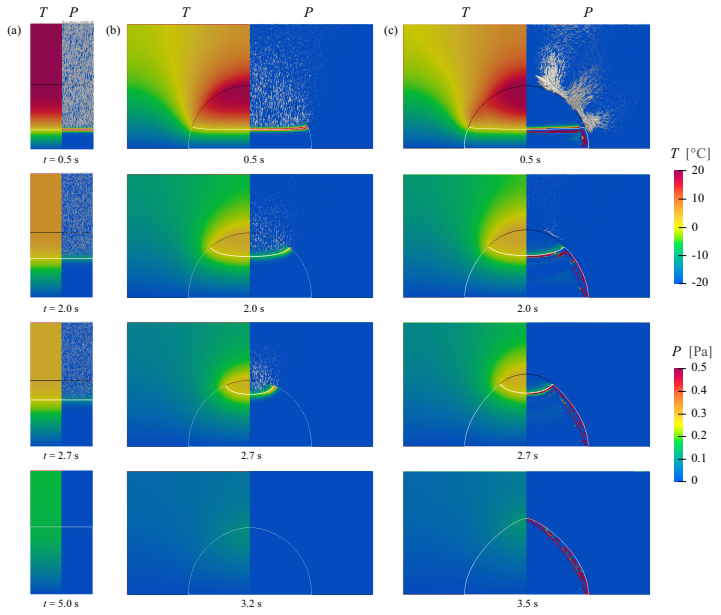

Fig. 21. The comparison of inner parameters between the freezing liquid film, the freezing drop without surface tension and gravity, and the freezing drop with surface tension and gravity. All figures are divided into two parts. The left parts show the temperature distributions and the right parts show the pressure distributions and the velocity fields. The ranges of temperature and pressure are shown in the right side of the figure. White lines show ice interfaces and black lines show liquid interfaces. (a) The first column shows the liquid film; (b) the second column shows the freezing drop without surface tension and gravity; (c) the third column shows the freezing drop with surface tension and gravity. For the first, second and third rows, each of them at the same time, but the fourth row corresponds to different final freezing moments t_f.

of the liquid film as $h_{li} = 1 \times 10^{-3}$m as shown in Fig. 21. The time step and the grid refinement are the same for the different simulations, $\Delta t/t_{diff} = 1.3 \times 10^{-6}$ and $\Delta/h_{li} = 6.7 \times 10^{-3}$. The contact angles of the drops are $\theta = 90°$. The numerical domain of the axisymmetric drop cases is a square with the length of 2×10^{-3} m.

In Fig. 21, each figure is divided into two parts. The temperature distributions are shown in the left part and the pressure and the velocity distributions are shown in the right part. The ranges of temperature and pressure are shown in the right side of the figure. The red area in the right parts shows the high pressure area where the pressure is larger than $P > 0.5$ Pa. The black lines show the gas-liquid interface, and the white lines show the solid interface. The arrows in the right part show the direction and magnitude of the velocity. The shapes of the solidification fronts for the liquid film and the drop are different due to the geometry. The solidification front of the liquid film is always flat but those of drops are curved. The temperature field is also significantly affected by the drop geometry resulting in a different rate of solidification as outlined by the comparison shown in the first, second and third rows where the time is the same for each row. The forth row reports the situations at the final freezing moment t_f. As shown when the initial height of liquid is the same, the freezing process is faster in the drop than in the liquid film because less and less liquid volume has to be iced with the same cold source.

We clearly observe in the right part of each figure the location of the maximum pressure at the (IBM)

solidification front and the velocity in the liquid phase caused by the expansion of the solidification when liquid freezes to ice, as described by Eqn. 25. In Fig. 21(b) (drop without surface tension and gravity), the direction of the velocity is not only vertical, but it is affected by the geometry of the drop. Because the magnitude of the velocity in the Fig. 21(c) (drop with surface tension and gravity) is much larger than those in the other two cases, the length of velocity arrows in the Fig. 21(c) reduces to be 2.5×10^{-3} times to be shown. Thus velocities of larger magnitude $v_{sp} \approx 10^{-3}$m/s develop close to the interface when the surface tension is considered. These velocities are the well-known spurious currents inherent to CSF methods [52, 26]. Considering the value of the Capillary number in our problem $Ca = \mu v_l/\sigma \approx 10^{-5}$, there are expected to develop and control the velocity field close to the interface. In the next section we discuss the influence of the spurious currents development on the icing simulation.

6.2. Spurious current characterization for the hybrid VoF-IBM method

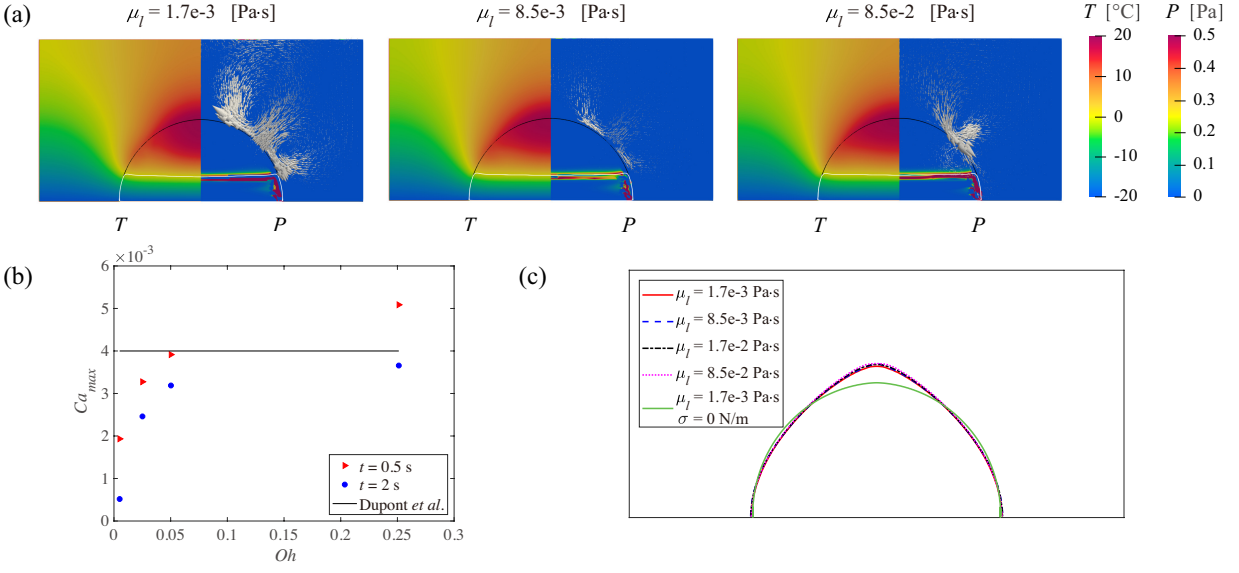

Fig. 22. By reducing the ratio σ/μ_l, the magnitude of the spurious currents can be reduced. (a) The freezing drops shape with surface tension and gravity but different viscosities of liquid at the moment $t = 0.5$ s. Each figure is divided into two parts. The left parts show the temperature distributions and right parts show the pressure distributions. The arrows show the direction and magnitude of the velocity. The scale bars of the velocity are the same for the first and second images. The velocity in the third image with the smaller viscosity is too small, so we enlarge the length of the arrow to 20 times for visualization. Maximum velocity are shown in (b) where the Capillary number based on the maximum velocity $Ca_{max} = \mu_l v_{max}/\sigma$ is reported as a function of the Ohnesorge number $Oh = \mu_l/\sqrt{\rho_l d_{eq} \sigma}$. The black line is $Ca = 0.004$ for the CSF-VoF method [53]. In (c) the final shape of the frozen drop with different viscosities compared to the freezing drop without surface tension and gravity.

The magnitude of the spurious currents observed in Fig. 21 (c) is known to increase with the ratio of the surface tension to viscosity σ/μ_l [53]. In order to study the effect of the development of the spurious current on the icing, we vary the ratio σ/μ_l by changing the viscosity of the liquid while keeping fixed the parameter controlling the drop icing such as the Bond number $Bo = \rho g d_{eq}^2/\sigma^2 = 0.34$, the contact angle $\theta = 90^o$, the Stefan number $Ste = 0.12$ number and the density ratio $\rho_s/\rho_l = 0.917$.

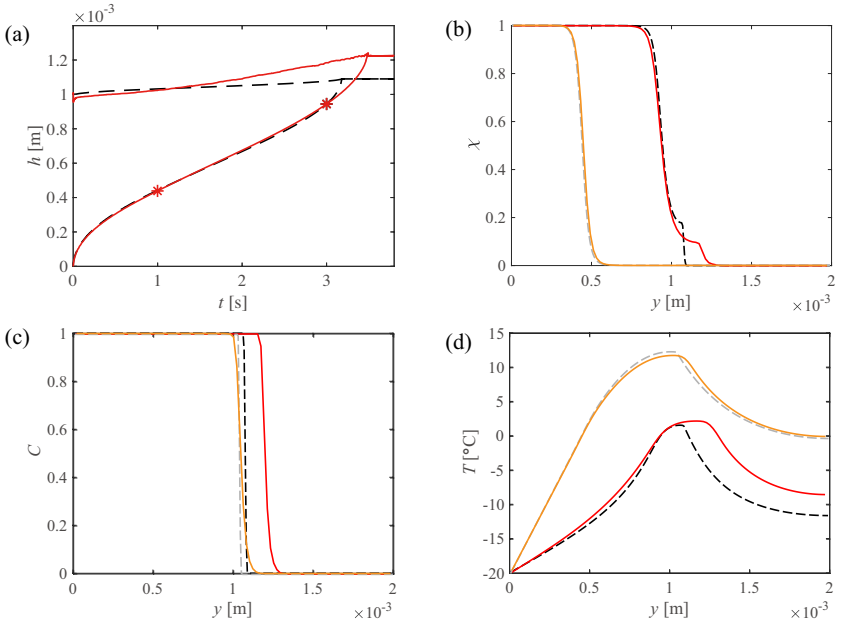

Fig. 23. Comparison between the drop without surface tension (dashed line) and gravity with the drop with surface tension and gravity (line). The inner parameter distributions are plotted along the symmetry axis at time $t = 1s$ (grey and orange) and $t = 3$s (black and red). (a) The evolution of the height of the gas-liquid and liquid-solid interfaces, red star show the two selected moments for the comparison, (b) the distribution of the χ function, (c) the distribution of the C function, (d) the distribution of the temperature.

In Fig. 22 (a), three freezing drops with different liquid viscosities at the moment $t = 0.5$ s are shown. Each figure is divided into two parts. The left parts show the temperature distributions and right parts show the pressure and velocity distributions. The red area in the right parts shows the high pressure area where the pressure is larger than $P > 0.5$ Pa. Both the temperature field and the pressure do not seem to be affected by the spurious currents magnitude. The arrows show the direction and magnitude of the corresponding velocity. The scale bars of the velocity are the same for the first and second images. The velocity in the third image is too small, so we enlarge the length of the arrow to 20 times for visualization. As expected, the magnitude of the spurious currents reduces with the increase of the viscosity μ_l. In Fig. 22 (b), the maximum velocity is shown using the Capillary number based on the maximum velocity $Ca_{max} = \mu_l v_{max}/\sigma$ reported as a function of the Ohnesorge number $Oh = \mu_l/\sqrt{\rho_l d_{eq} \sigma}$. The magnitude of the spurious current observed for the IBM-VoF-CSF methods are found to be of same order of magnitude of the spurious velocities measured in the original VoF method in JADIM [53, 54] where the spurious velocities evolve as $0.004\ \sigma/\mu_l$. The final shape of the frozen drops is reported in Fig. 22 (c) for the different viscosities considered. As shown the final shape of the drop is not impacted by the development of the spurious currents, a result consistent with the small values of both the Weber and Capillary numbers.

Therefore, we choose the drop with larger viscosity to investigate the inner parameter distributions. In Fig. 23, the viscosity of liquid is $\mu_l = 8.5 \times 10^{-2}$ Pa·s. The selected times are $t = 1$s and $t = 3$s, the later being close to the end of the solidification. Comparing to the freezing drops without surface tension and

gravity, the main difference is related to the evolution of the gas-liquid interface. In Fig. 23(a) the final height of the drop becomes larger due to the surface tension effect as described above and the corresponding freezing time is larger. Other distributions appears to have similar shapes and are not affected along the drop axis line by the geometry change due to surface tension.

6.3. Comparison with experiments

In order to further confirm the accuracy of the numerical method, we compare the numerical result with the experimental result. Firstly, we compare the final profile of the frozen drop in the Fig. 24. Marín *et al.*[3] experimentally measured the final profile of frozen drops with different contact angles. We use the drop with the contact angle 90° from Marín *et al.*[3] for the comparison reported in the Fig. 24. The magenta line shows the numerical result obtained considering surface tension and gravity. We find that the numerical result fits well with the experimental results. In addition, we compare the tip angles in the Table. 5. We find the tip angle for drops with the consideration of surface tension and gravity forces fits well with the experimental result, while the tip angles for the simulation of the drops without considering those forces were found larger (see previous section). Thus we show that the effect of gravity and surface tension are very essential so that one can not ignore them in the solidification process.

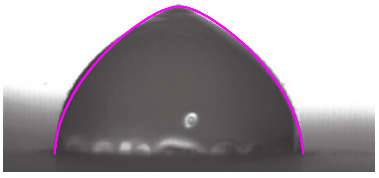

Fig. 24. The final numerical profile of frozen drop shown as the magenta line fits with the experimental result.

Table 5. The tip angle α of frozen drops

Case	Without surface tension and gravity	With surface tension and gravity	Experiment
Tip angle α [°]	170	139	141

In addition, we also study the front-to-interface angle γ, which is shown in Fig. 25(a). We recall, that the angle between the three phases is not imposed but results from the local solidification isotherm $T = T_m$ so that it is controlled by the balance of the heat fluxes from the three phases. In particular, in the situation of no flux exchange with the external air, an angle of 90^o is observed. We detail the method used for the angle calculation in the cells where the three phases are present. In the Fig. 25(a), magenta points show the solid-liquid interface corresponding to the solidification isotherm $T = T_m$, and blue points show the drop-gas interface corresponding to the VoF function value $C = 0.5$. The zoom figure of the green square is shown on the right. γ is defined as the angle in the solid area between the solid-liquid interface and the solid-gas interface. We use the slopes of the red line and the black line to calculate the value of γ, which

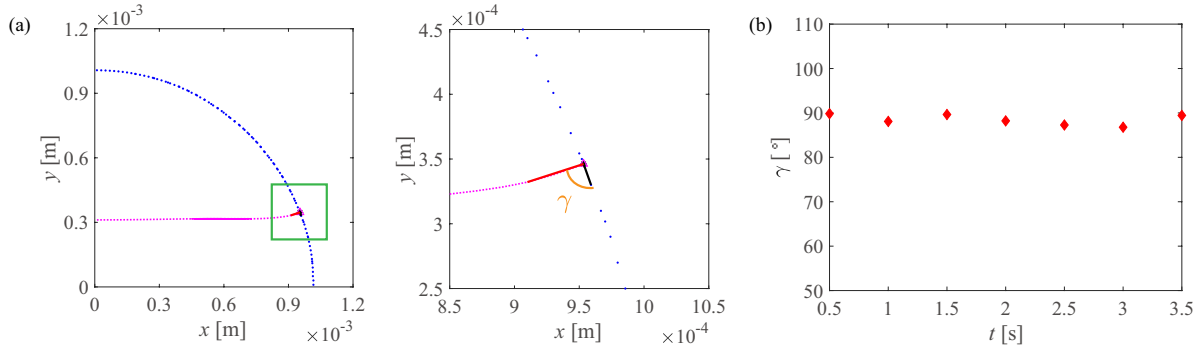

Fig. 25. The angle γ in the solid area between the solid-liquid interface and the solid-gas interface. (a) Magenta points show the solid-liquid interface. Blue points show the drop-gas interface. The zoom figure of the green square is shown in the right. γ is defined as the angle in the solid area between the solid-liquid interface and the solid-gas interface. (b) γ evolution as time t.

is plotted in Fig. 25(b). γ is nearly a constant equals 90°. Note that the front-to-interface angle γ is not impacted by considering the surface tension; a value close to $\gamma \approx 90°$ is in agreement with the experimental result [3], which results from the poor relative conductivity of the gas as discussed above.

7. Conclusion

In this work, we present and validate the development of a hybrid VoF-IBM method for the simulation of the icing of liquid drop and liquid film. The VoF and IBM methods of JADIM are coupled with the temperature equation to be able to solve the icing front, the dilatation induced by the density difference between the liquid and the ice, as well as the deformation induced by the balance of surface tension and gravity at the gas-liquid interface. Firstly we compare the liquid film solidification with the Stefan theoretical solution to check the applicability and accuracy of JADIM. The tests are performed for different density ratios and different initial conditions. Then we apply JADIM to investigate the freezing dynamics of drops. Through comparing the results of the liquid film and drops, we investigate the effects of several important parameters, such as the ratio between the solid density to the liquid density, the initial conditions, the contact angle of the drop. We show that the freezing time t_f of the drop is increased with the decrease of the Stefan number Ste, the decrease of the density ratio and the increase of the drop contact angle providing convex solidification front. Furthermore, we study the effect of the gravity and the surface tension on the drop freezing processes. In particular we discuss the CSF-VoF spurious currents and we show that they induce no effect on the icing process due to the small value of the induced Weber and Capillary numbers. We find that the final ice shape is in a very good agreement with experiments, and in particular the value of the tip angle of the iced drop and the front-to-interface angle are satisfactorily reproduced. Our method has been validated on simple configurations, and more unstable cases as dendritic growths will be considered in the future.

Acknowledgments

We are really grateful to Saverio Buccini, Francesco Peccianti and Ariane Perelle Kamdem Paula for the help in developing the hybrid IBM-VoF method in JADIM. We also thanks Thomas Bonometti for fruitful discussions related to the IBM method. This work was supported by Natural Science Foundation of China under grant no 11861131005, and Tsinghua University Initiative Scientific Research Program under grant no 20193080058.

References

[1] J. H. Snoeijer, P. Brunet, Pointy ice-drops: how water freezes into a singular shape, American Journal of Physics 80 (2012) 764–771.
[2] S. Wildeman, S. Sterl, C. Sun, D. Lohse, Fast dynamics of water droplets freezing from the outside in, Physical review letters 118 (2017) 084101.
[3] A. G. Marin, O. R. Enriquez, P. Brunet, P. Colinet, J. H. Snoeijer, Universality of tip singularity formation in freezing water drops, Physical review letters 113 (2014) 054301.
[4] L. Boinovich, A. M. Emelyanenko, V. V. Korolev, A. S. Pashinin, Effect of wettability on sessile drop freezing: when superhydrophobicity stimulates an extreme freezing delay, Langmuir 30 (2014) 1659–1668.
[5] M. F. Ismail, P. R. Waghmare, Universality in freezing of an asymmetric drop, Applied Physics Letters 109 (2016) 234105.
[6] G. Chaudhary, R. Li, Freezing of water droplets on solid surfaces: An experimental and numerical study, Experimental Thermal and Fluid Science 57 (2014) 86–93.
[7] M. Nauenberg, Theory and experiments on the ice-water front propagation in droplets freezing on a subzero surface, Eur. J. Phys. 37 (2016) 045102.
[8] L. Huang, Z. Liu, Y. Liu, Y. Gou, L. Wang, Effect of contact angle on water droplet freezing process on a cold flat surface, Experimental Thermal and Fluid Science 40 (2012) 74–80.
[9] M. Theillard, F. Gibou, T. Pollock, A sharp computational method for the simulation of the solidification of binary alloys, Journal of scientific computing 63 (2015) 330–354.
[10] G. Comini, S. Del Guidice, Finite element solution of non linear heat conduction problems with special reference to phase change, J. Numer. Meth. Eng. 8 (1974) 613–624.
[11] V. R. Voller, C. R. Swaminathan, B. G. Thomas, Fixed grid techniques for phase change problems: a review, International Journal for Numerical Methods in Engineering 30 (1990) 875–898.
[12] R. Viswanath, Y. Jaluria, A comparison of different solution methodologies for melting and solidification problems in enclosures, Numer. Heat Transfer 24 (1993) 77–105.
[13] C. K. Chiu, J. Caldwell, Application of broyden's method to the enthalpy method for phase change problems, Numerical Heat Transfert 30 (1996) 575–587.
[14] J. A. Makenzie, M. L. Robertson, G. Beckett, A moving mesh finite element method for the solution of two-dimensional, Journal of Computational Physics 168 (2001) 500–518.
[15] T. Vu, G. G.Tryggvason, S. Hommac, J. Wells, Numerical investigations of drop solidification on a cold plate in the presence of volume change, International Journal of Multiphase Flow 76 (2015) 73–85.
[16] X. Zhang, X. Liu, W. Xiaomin, M. Jingchun, Simulation and experiment on supercooled sessile water droplet freezing with special attention to supercooling and volume expansion effects, International Journal of Heat and Mass Transfer 127 (2018) 975–985.
[17] M. Tembely, A. Dolatabadi, A comprehensive model for predicting droplet freezing features on a cold substrate, Journal of Fluid Mechanics 859 (2019) 566–585.
[18] M. Lepilliez, E. R. Popescu, F. Gibou, S. Tanguy, On two-phase flow solvers in irregular domains with contact line, Journal of Computational Physics 321 (2016) 1217–1251.
[19] H.-R. Li, H.-L.and Liu, D. H., A fully 3d simulation of fluid-structure interaction with dynamic wetting and contact angle hysteresis, Journal of Computational Physics 109709 (2020).
[20] J. Dupont, D. Legendre, Numerical simulations of static and sliding drop with contact angle hysteresis, Journal of Computational Physics 229 (2010) 2453–2478.
[21] D. Legendre, M. Maglio, Numerical simulation of spreading drops, Colloids and Surfaces A: Physicochemical and Engineering Aspects 432 (2013) 29–37.
[22] D. Legendre, M. Maglio, Comparison between numerical models for the simulation of moving contact lines, Computer and Fluids 113 (2015) 2–13.
[23] B. Bigot, T. Bonometti, L. Lacaze, O. Thual, A simple immersed-boundary method for solid-fluid interaction in constant- and stratified -density flows, Computers and Fluids 97 (2014) 126–142.
[24] V. R. Voller, C. R. Swaminathan, General source-based method for solidification phase change, Numerical Heat Transfert 19 (1991) 175–189.
[25] T. Bonometti, J. Magnaudet, An interface capturing method for incompressible two-phase flows. validation and application to bubble dynamics, International Journal of Multiphase Flow 33 (2007) 109–133.
[26] T. Abadie, J. Aubin, D. Legendre, On the combined effects of surface force calculation and interface advection on spurious currents within volume of fluid and level set frameworks, Journal of Computational Physics 297 (2015) 611–636.

[27] H. Si Hadj Mohand, H. Hoang, G. Galliero, D. Legendre, On the use of a friction model in a volume of fluid solver for the simulation of dynamic contact lines, Journal of Computational Physics 393 (2019) 29–45.
[28] M. Vahab, C. Pei, M. Y. Hussaini, M. Sussman, Y. Lian, An adaptive coupled level set and moment-of-fluid method for simulating droplet impact and solidification on solid surfaces with application to aircraft icing, American Institute of Aeronautics and Astronautics 54th AIAA Aerospace Sciences Meeting (2016) 1340.
[29] Y. Yuki, S. Takeuchi, T. Kajishima, Efficient immersed boundary method for strong interaction problem of arbitrary shape object with self-induced flow, J Fluid Sci Tech 2 (2007) 1–11.
[30] E. Fadlun, R. Verzicco, P. Orlandi, J. Mohd-Yusof, Combined immersed-boundary infinite-difference methods for three-dimensional complex flow simulations, Journal of Computational Physics 161 (2000) 35–60.
[31] M. Uhlmann, An immersed boundary method with direct forcing for the simulation of particulate flows, Journal of Computational Physics 209 (2005) 448–476.
[32] I. Calmet, J. Magnaudet, Large-eddy simulation of high-schmidt number mass transfer in a turbulent channel flow, Physics of Fluids 9 (1997) 438–455.
[33] D. Legendre, J. Magnaudet, The lift force on a spherical body in a viscous linear shear flow, J. Fluid Mech. 368 (1998) 81–126.
[34] J. Magnaudet, M. Rivero, J. Fabre, Accelerated flows past a rigid sphere or a spherical bubble. part 1. steady strainning flow, J. Fluid Mech. 284 (1995) 97–135.
[35] D. Legendre, J. Magnaudet, G. Mougin, Hydrodynamic interactions between two spherical bubbles rising side by side in a viscous liquid, J. Fluid Mech. 497 (2003) 133–166.
[36] A. Merle, D. Legendre, J. Magnaudet, Forces on a high-re spherical bubble in a turbulent flow, J. Fluid Mech. 532 (2005) 53–62.
[37] Y. Hallez, D. Legendre, Interaction between two spherical bubbles rising in a viscous liquid, J. Fluid Mech. 673 (2011) 406–431.
[38] A. Atasi, B. Haut, A. Pedrono, B. Scheid, D. Legendre, Influence of soluble surfactants and deformation on the dynamics of centered bubbles in cylindrical microchannels, Langmuir 34 (2018) 10048–10062.
[39] D. Legendre, A. Rachih, C. Souilliez, S. Charton, E. Climent, The Basset-Boussinesq history force of a fluid sphere, Physical Review Fluids 4 (2019) 073603.
[40] M. Maglio, D. Legendre, Numerical simulation of sliding drops on an inclined solid surface, in: Computational and Experimental Fluid Mechanics with Applications to Physics, Engineering and the Environment, Springer, 2014, pp. 47–69.
[41] S. H. Davis, Theory of solidification, Cambridge University Press, 2001.
[42] J. C. Jaeger, H. S. Carslaw, Conduction of heat in solids, Clarendon P, 1959.
[43] E.-i. Hanzawa, Classical solutions of the stefan problem, Tohoku Mathematical Journal, Second Series 33 (1981) 297–335.
[44] V. Voller, M. Cross, Accurate solutions of moving boundary problems using the enthalpy method, International journal of heat and mass transfer 24 (1981) 545–556.
[45] V. Voller, An implicit enthalpy solution for phase change problems: with application to a binary alloy solidification, Applied Mathematical Modelling 11 (1987) 110–116.
[46] J. Caldwell, C.-C. Chan, Spherical solidification by the enthalpy method and the heat balance integral method, Applied Mathematical Modelling 24 (2000) 45–53.
[47] A. Date, Novel strongly implicit enthalpy formulation for multidimensional stefan problems, Numerical Heat Transfer, Part B Fundamentals 21 (1992) 231–251.
[48] W. G. Habashi, et al., Development of a second generation in-flight icing simulation code, Journal of fluids engineering 128 (2006) 378–387.
[49] C. Zhang, H. Liu, Effect of drop size on the impact thermodynamics for supercooled large droplet in aircraft icing, Physics of Fluids 28 (2016) 062107.
[50] P. Ke, X. Wang, Super-cooled large droplets consideration in the droplet impingement simulation for aircraft icing, Procedia Engineering 17 (2011) 151–159.
[51] S. F. Ahmadi, S. Nath, C. M. Kingett, P. Yue, J. B. Boreyko, How soap bubbles freeze, Nature communications 10 (2019) 2531.
[52] J. Brackbill, D. Kothe, C. Zemach, A continuum method for modeling surface tension, Journal of Computational Physics 100 (1992) 335–354.
[53] J.-B. Dupont, D. Legendre, Numerical simulation of static and sliding drop with contact angle hysteresis, Journal of Computational Physics 229 (2010) 2453–2478.
[54] T. Abadie, J. Aubin, D. Legendre, On the combined effects of surface tension force calculation and interface advection on spurious currents within volume of fluid and level set frameworks, Journal of Computational Physics 297 (2015) 611–636.